The Effects of Burial Diagenesis on Multiscale Porosity in the St. Peter Sandstone: An Imaging, Small-Angle, and Ultra-Small-Angle Neutron Scattering Analysis

Lawrence M. Anovitz*[a], Jared T. Freiburg [b,c], Matthew Wasbrough [d], David F. R. Mildner [d], Kenneth C. Littrell [e], Vitaliy Pipich [f] , Jan Ilavsky [g]

for submission to *Marine and Petroleum Geology*
Draft of April 24, 2017

[a] Chemical Sciences Division, MS 6110, Oak Ridge National Laboratory, Oak Ridge, TN 37831-6110, United States, anovitzlm@ornl.gov
[b] Illinois State Geological Survey, University of Illinois, 615 E. Peabody, Champaign, IL 61820, United States, freiburg@illinois.edu
[c] Ernst-Moritz-Arndt-University, Institute of Geography and Geology, Friedrich-Ludwig-Jahn Str. 17a, D-17489 Greifswald, Germany
[d] NIST Center for Neutron Research, Stop 8562, Gaithersburg, MD 20899, United States, mildner@nist.gov, matthew@wasbrough.co.uk
[e] Chemical & Engineering Materials Division, MS 6393, Oak Ridge National Laboratory, Oak Ridge, TN 37831-6393, United States, littrellkc@ornl.gov
[f] Jülich Centre for Neutron Science JCNS, Forschungszentrum Jülich GmbH, Outstation at MLZ, Lichtenbergstr.1, 85747 Garching, Germany, v.pipich@fz-juelich.de
[g] Argonne National Laboratory, 9700 S. Cass Ave., Bldg. 433A, Argonne, IL 60439, United States
*Corresponding author

ABSTRACT

To examine the effects of burial diagenesis on heirarchical pore structures in sandstone and compare those with the effects of overgrowth formation, we obtained samples of St. Peter Sandstone from drill cores obtained in the Illinois and Michigan Basins. The multiscale pore structure of rocks in sedimentary reservoirs and the mineralogy associated with those pores are critical factors for estimating reservoir properties, including fluid mass in place, permeability, and capillary pressures, as well as geochemical interactions between the rock and the fluid. The combination of small- and ultra-small-angle neutron scattering with backscattered electron or X-ray-computed tomographic imaging, or both, provided a means by which pore structures were quantified at scales ranging from aproximately 1 nm to 1 cm—seven orders of magnitude. Larger scale (>10 μm) porosity showed the expected logarithmic decrease in porosity with depth, although there was significant variation in each sample group. However, small- and ultra-small-angle neutron scattering data showed that the proportion of small-scale porosity increased with depth. Porosity distributions were not continuous, but consisted of a series of log normal-like distributions at several distinct scales within these rocks. Fractal dimensions at larger scales decreased (surfaces smoothed) with increasing depth, and those at smaller scales increased (surfaces roughened) and pores become more isolated (higher lacunarity). Data suggest that changes in pore-size distributions are controlled by both physical (compaction) and chemical effects (precipitation, cementation, dissolution).

1. INTRODUCTION

The study of sandstones was one of the earliest efforts in the geological sciences, dating back at least to the work of James Hutton, John Playfair, Roderick Murchison, and Adam Sedgwick on the Old Red Sandstone (Hutton, 1788; Playfair, 1802; Sedgewick and Murchison, 1840). Dott (1964) provided a classic method to characterize sandstones, based in part on the earlier work of Gilbert (in Williams et al., 1954) and Folk (1951, 1961). Although "sand" is formally a term that refers to a range of grain sizes, Pettijohn et al. (2012) noted that the term "sandstone" is typically restricted to " those indurated sands of siliceous character."

Although one typically thinks of sandstone in terms of its mineral grains, its porosity and permeability makes it important as natural and potential anthropogenic storage sites. Understanding the pore structures of sandstones is, therefore, critical to understanding a wide range of processes: the evolution of aquifers; properties of dimension stone, flagstone, and crushed stone; formation of and energy recovery from oil and gas reservoirs; and geological CO_2 sequestration. Although much work has been undertaken to understand and quantify sandstone porosity (cf. Freiburg et al., 2016), studies of submicron porosity have typically been limited by the difficulty of quantifying pore structures at the smallest scales. Whereas submicron pore structures are easily observed using transmission electron microscopy and high-resolution scanning electron microscopy (SEM), the large magnifications involved limit the volumes investigated, and thus the ability of such approaches to quantify pore structures at these scales.

Despite the obvious importance of larger-scale pores to sandstone structures available data suggest these smaller pores are an important compotent of the overall pore structure. In fact, it is likely these finer-scale features control much of the flow dynamics in sandstones, and can be significantly impacted by diagenetic events. Pettijohn et al. (2012) commented:

> The grains in a sand are generally in tangential contact only and thus form an open, three-dimensional network. As a consequence, sands have a high porosity—have a fluid-filled pore system. The unequal distribution of stress along grain boundaries may lead to solution at points of pressure and deposition elsewhere increasing the surfaces of contact and decreasing the pore space. Such action, coupled in some cases with the introduction of cementing materials, leads to the ultimate end-product—a rock with grains in continuous contact and without porosity. In this manner, a sand with tangential contacts and a porosity of 35 to 40 percent is converted to an interlocking crystalline mosaic with zero porosity. (p. 1)

While this clearly describes the overall evolution of many sandstones, the claim that sandstones progress to zero porosity is somewhat overstated. In our previous studies (Anovitz et al., 2013a, 2015a), for example, we showed that low-pressure silcrete formation the St. Peter Sandstone from southwest Wisconsin, while lowering total porosity, decreasing pore size, and making the remaining pores more isolated, did not eliminate porosity altogether, and tended to make the smaller pores volumetrically more significant. Available data suggest, however, that these samples had never been buried to great depths (Hoholick et al., 1984; Mai and Dott, 1985; Rowan and Goldhaber, 1996; Pitman et al., 1997; Prothero and Dott, 2004; Kelly, 2006; Kelly et al., 2007; Anovitz et al., 2013a). Thus, although these samples allowed us to evaluate the effects of precipitation on porosity, a different sample suite was needed to extend this analysis to basinal diagenesis. The focus of this paper, therefore, is to evaluate changes in the pore structure of the St. Peter Sandstone from the Illinois and Michigan Basins with burial. We have done so by combining imaging analysis at larger scales, with small and ultrasmall angle neutron scattering to characterize pore structures over a seven order of magnitude range, from the centimeter to the nanometer scale.

1.1. Geology

The Middle Ordovician St. Peter Sandstone, part of the Ancell Group, covers wide areas of the U.S. Midcontinent (Dake, 1921; Dapples, 1955). The earliest work on the St. Peter was probably that of Owen (1847), who named it for the Minnesota River, which was then called the St. Peter River. It is found in both the Illinois and Michigan Basins, which formed in response to far-field plate tectonic effects (Hinze et al., 1988). The St. Peter is a super-mature quartz arenite (<99% quartz) that consists primarily of well-sorted, fine to medium, well-rounded quartz grains. Abundant primary and secondary porosity are presently associated with major diagenetic controls, such as compaction, cementation, and dissolution. Reported porosity ranges from 30% in outcrop to virtually zero at 8000 ft (2438 m) in the Illinois Basin (Hoholick et al., 1984), although the latter likely omits significant fine-scale porosity.

The St. Peter Sandstone was deposited in an advancing marine shoreline dominated by eolian dune and beach processes (Kolata, 2010). It covers most of the Illinois Basin uniformly, except in areas of underlying surface irregularities attributable to karst topography (Collinson et al., 1988). It is much more variable in thickness and occurrence in the Michigan Basin, also partially due to deposition on a karst surface (Fisher et al., 1988). The St. Peter is most commonly 100 (30 m) to 200 feet (61 m) thick in the Illinois Basin and can be up to 1200 feet (366 m) thick in the Michigan Basin (Barnes et al., 1992). Depths in the Illinois Basin range from the surface in southwest Wisconsin (see Kelly, 2006; Kelly et al., 2007; Anovitz et al., 2013a) to nearly 7000 feet (2134 m). In the Michigan Basin, the St. Peter occurs at depths ranging from less than 1000 feet (305 m) in the southeastern Upper Peninsula (Mackinac County) to greater than 10,000 feet (3048 m) near the center of the basin (Zdan, 2013).

Since the deposition of the St. Peter Sandstone, the basins have experienced several episodes of subsidence and uplift (Kolata and Nelson, 2010). By the Late Permian in the Illinois Basin, the St. Peter was buried to a maximum depth of approximately 4500–6000 feet (~1372–1829 m) in southern Illinois, based on data of the top of the Mt. Simon Sandstone (Makowitz et al., 2006). However, burial reconstruction by Pitman et al. (1997) has the St. Peter attaining a burial and temperature maximum (3.3 km and 140 °C) during the Late Pennsylvanian and Early Permian periods, coincident with regional Permian igneous activity and ore-forming events (Mississippi Valley-type [MVT] deposits). Others have suggested a geothermal gradient of 10–110 °C/km (Kelly et al., 2007; Pollington et al., 2011) based on oxygen isotopes and fluid inclusion data of quartz overgrowths in the Mt. Simon Sandstone (Fishman, 1997) and other burial models (Makowitz et al., 2006). In the Michigan Basin near the end of the Carboniferous Period, the St. Peter was buried to a maximum depth of 13,000 feet (~4 km), based on thermal maturity analyses of organics (Cercone, 1984). An elevated thermal gradient of 34–60 °C/km during the Paleozoic has been suggested (Girard and Barnes, 1995; Graham et al., 1996), likely related to a buried Precambrian rift in the center of the basin (Cercone and Pollack, 1991).

The diagenetic history of the St. Peter in the Illinois (Hoholick et al., 1984; Pitman et al., 1997) and Michigan Basins (Barnes et al., 1992; Drzewiecki et al., 1994; Zdan, 2013) has been studied thoroughly. In the Illinois Basin, multiple generations of authigenic minerals occur, contributing to an associated variability in porosity (Pitman et al., 1997). Authigenic K-feldspar emplacement occurred in the Devonian Period at approximately 400 Ma during early diagenesis at relatively shallow depths (<1,500 m) and low temperatures of ~65 °C (Krueger and Woodard, 1972; Marshall et al., 1986; Elliott and Aronson, 1987, 1993; Hay et al., 1988; Sweeney and Burnham, 1989; Lee and Aronson, 1991; Barnes et al., 1992; Hay and Liu, 1994; Pitman and

Spöetl, 1996; Pitman et al., 1997). Multiple generations of illite formed, and similar generations are observed in older clastic rocks in the Illinois Basin that likely contribute significant microporosity (Freiburg et al., 2014). Compared with K-feldspar emplacement, illite precipitation occurred over a wider time frame (360 to 215 Ma; Hay et al., 1988; Lee and Aronson, 1991; Grathoff et al., 2001; Elliott and Aronson, 1993). Authigenic quartz forms optically continuous but complex, concentrically zoned (under cathodoluminescent light), synaxial overgrowths on detrital quartz grains and postdates diagenetic illite and feldspar (Pitman et al., 1997; Kelly et al., 2007; Anovitz et al., 2015a). Isotopic studies suggest quartz precipitation at low and relatively homogeneous temperatures (10–30 °C; Graham et al., 1996; Kelly et al., 2007). Other studies of quartz overgrowths in underlying formations such as the Eau Claire (Hyodo et al., 2013) and Mt. Simon (Pollington et al., 2011) suggest that multigenerational quartz cementation formed in response to increased temperatures during burial. Carbonate cements in the St. Peter include dolomite and calcite and are largely segregated to the east-central and southern portions of the Illinois Basin (Hoholick et al., 1984; Pitman et al., 1997). These are attributed to hydrothermal fluids similar to MVT brines based on stable isotopes and fluid inclusion temperatures and salinities. Isotopic analyses in the underlying Eau Claire Formation suggest cements formed in response to progressive sediment burial and heating, with final temperatures consistent with mid-Permian MVT brines (Sliwinski et al., 2016). Anhydrite was the last major diagenetic cement to form in the St. Peter. It is largely segregated to the depocenter of the Illinois Basin in southeastern Illinois and southwestern Indiana, and it is inferred anhydrite was deposited during the maximum burial of the St. Peter (Pitman et al., 1997). Other controls on porosity include mechanical and chemical compaction, cement dissolution, framework detrital grain dissolution, and fracturing (Hoholick et al., 1984).

In the Michigan Basin, authigenic minerals in the St. Peter are relatively consistent throughout the central basin (Barnes et al., 1992). Barnes et al. (1992) suggest that no significant variation in diagenetic alteration occurs as a function of burial depth, but that a relationship to primary mineralogy is influenced by variable depositional environments. This differs from the Illinois Basin, where cements are depth dependent and define distinct regions (Hoholick et al., 1984). However, isotopic and fluid inclusion analyses of cathodoluminescent zoned quartz overgrowths in the Michigan Basin suggest precipitation occurred over a range of temperatures (Girard and Barnes, 1995; Graham et al., 1996), implying a relationship to burial depth. Illitization of the St. Peter in the Michigan Basin appears to have some overlap with that in the Illinois Basin but with a shorter window during the Late Devonian to Mississippian periods (367–322 Ma; Girard and Barnes, 1995). As in the Illinois Basin, porosity is significantly controlled by compaction and dissolution of both authigenic and framework minerals.

1.2. Sample Locations

For this study, samples were recovered from whole and sidewall cores from four Illinois wells and one from Michigan. The Illinois wells were drilled in an approximately north–south line. In the first, C-28 (API no. 121670011500), located in Sangamon County, Illinois, township 15N, range 3W, section 11, samples were recovered from 2703-2732 feet (820-830 m). In the second, C-13368 (API no. 121350176000), located in Montgomery County, township 9N, range 3W, section 6, samples were recovered from 3155–3309 feet (962–1009 m). In the third, C-228 (API no. 120270055701), samples were recovered from 4117-4119 4100 feet (1254.9-1255.5 m). It was located in Clinton County, Illinois, township 2N, range 3W, section 3. In the fourth, C-4831 (API no. 121210519800), samples were recovered from 5239-5250 feet (1590-1600 m). It was located in Marion County, township 1N, range 2E, section 6. In the well from the Michigan Basin, Briggs

unit (API no. 21011398890000), located in Arenac County in township 20N, range 4E, section 12, samples were recovered from 10,816 and 10835 feet (3290-3300 m).

2. ANALYTICAL APPROACHES

In our previous work (Anovitz et al., 2013a, 2015a), we have shown that porosity in sandstones is highly heirarchical, with pores ranging in size from nanometers to millimeters or larger. Although traditional optical and electron imaging techniques can provide much information on sandstone porosity, especially when abetted by petrophysical approaches (cf. Anovitz and Cole, 2015), a different approach is required to extend quantitative analyses over a wide range of scales. To do so, we have combined four techniques: small-, very-small and ultra-small-angle neutron scattering (SANS, USANS, VSANS), and backscattered electron imaging (BSE)/SEM to quantify porosity on length scales from ~1 nm to ~1 cm, a seven-decade range.

Details of the analytical approaches have been reported elsewhere (Anovitz et al., 2009, 2011, 2013a,b, 2015a,b; Wang et al., 2013) and are, therefore, summarized briefly. SANS, VSANS and USANS were used to probe porosity over length scales from ~10 nm to 30 μm. This was expanded to ~1 cm using the autocorrelation functions calculated from BSE images at 14×. Neutron scattering measurements were performed on thin sections (0.15 mm thick) mounted on 1-mm-thick quartz glass slides with the beam incident along the surface normal. SANS measurements were conducted on the general purpose SANS instrument at the High Flux Isotope Reactor at the Oak Ridge National Laboratory (Littrell et al., 2008) using a 6-mm mask. Three sample-to-detector distances (1.1, 4.7, and 19.3 m) were used with λ = 4.75 Å at 1.1 and 4.7 m, and 19 Å at 19.3 m, with a wavelength resolution $\Delta\lambda/\lambda$ = 0.14. Measurements were performed with the detector offset to extend the range of the scattering vector Q ($Q = 2\pi/d$) at each setting

and provide better overlap. The resultant scattering vector ranged from 0.0009 to 0.9 $Å^{-1}$, which corresponds to sizes from ~7 to 7000 Å. Data were corrected for empty-beam scattering, background counts, detector uniformity, sample transmission and scattering volume, and reduced to an absolute scale (differential scattering cross-section per unit volume) by normalization to the intensity of the direct beam. The two-dimensional data were always azimuthally symmetric, and were circularly averaged to produce one-dimensional intensity profiles.

Ultra-small-angle neutron scattering measurements were performed on the BT5 instrument at the Center for Neutron Research at the National Institute of Standards and Technology (Barker et al., 2005). Samples were mounted on 1/2- or 5/8-inch cadmium masks. A pair of triple-bounce channel-cut perfect silicon (220) crystals was used for the monochromator and analyzer. The wavelength was 2.38 Å with a wavelength resolution $\Delta\lambda/\lambda = 0.059$. Data were collected over a Q range from 4.2×10^{-5} to 2.7×10^{-3} $Å^{-1}$, which corresponds to sizes from2400 Å to ~15 μm. The horizontal Q resolution (full width at half maximum) was 2.5×10^{-5} $Å^{-1}$. Scattering intensity data were corrected for empty beam and constant background levels. The corrected data were converted to an absolute scale by measuring the attenuation of the direct beam through the sample. Further data reduction and desmearing were accomplished through the USANS data reduction software provided by NIST/NCNR (Kline, 2006).

Very-small-angle neutron scattering experiments were performed on the KWS-3 instrument at the Forschungs-Neutronenquelle Heinz Maier-Leibnitz (FRM II) in Munich, Germany. This instrument uses a focusing mirror geometry to cover a Q range intermediate between SANS and USANS. Samples were run for 1.5 hours in the 9.5-meter position, covering a scattering vector range between 4.0×10^{-5} $Å^{-1}$ and 2.5×10^{-3} $Å^{-1}$ (Alefeld et al., 1997, 2000a,b). Absolute intensities were adjusted to fit the SANS and USANS data.

Backscattered electron images of the pore space were used to extend the scattering curve to larger scales and to provide two-dimensional information on the lacunarity and multifractal spectrum of the pore system (Debye et al., 1957; Anovitz et al., 2013a, 2105a; Wang et al., 2013). Images were obtained using a Hitachi S3400 environmental SEM. The samples were not coated, and a pressure of 50 Pa was used to eliminate charging. Images were obtained at 14x. Each image consisted of 5120 × 3840 pixels, and the pixel edge length was 1.772 μm. Thus, the pixel size overlapped the maximum USANS scale by approximately one order of magnitude.

3. RESULTS

3.1. Sample Petrography

Ten sections were prepared from cores from the wells described above for petrographic analysis. Thin sections were impregnated with blue epoxy to identify porosity. Petrographic analyses included plane-light and cathodoluminescence microscopy. Mineral composition and porosity were quantified using standard point-counting methods (typically 300 points per thin sections) and image analysis software (Olympus Stream). Results are shown in Table 1.

Porosity and diagenesis vary significantly in the samples examined. Samples from well C-28 in Sangamon County, Illinois were well-sorted quartz arenites predominantly composed of lightly consolidated and compacted, medium to fine, well-rounded quartz grains. Authigenic clay cement was partially abundant throughout with rare authigenic quartz and dolomite cements. Porosity was largely a primary framework with minor secondary cement and complete grain dissolution. Porosity was measured from 6.2 to 30.2% in thin section. Samples from well C-13368 in Montgomery County, Illinois were moderately well-sorted quartz arenites predominantly composed of moderately consolidated, lightly compacted, medium to fine, rounded to well-

rounded quartz grains. Authigenic quartz overgrowths were common, and dolomite and clay cements were rare. Porosity was largely a primary stable framework with significant secondary contribution from unknown dissolved detrital grains and ranged from 16.8 to 29.7% in a thin section. Samples from well C-228 in Clinton County, Illinois were moderately to poorly sorted quartz arenites predominantly composed of moderately consolidated, lightly compacted, coarse to silt-size, rounded to subangular quartz grains. The sample recovered from 4118 feet (1.26 km) had abundant fine-grained dolomite cement with rare, later, coarser euhedral dolomite rhombohedra. Authigenic quartz overgrowths and clay cements were relatively rare throughout. Porosity varied from 14.8 to 21.5% in thin section, and was largely a stable framework with moderate secondary

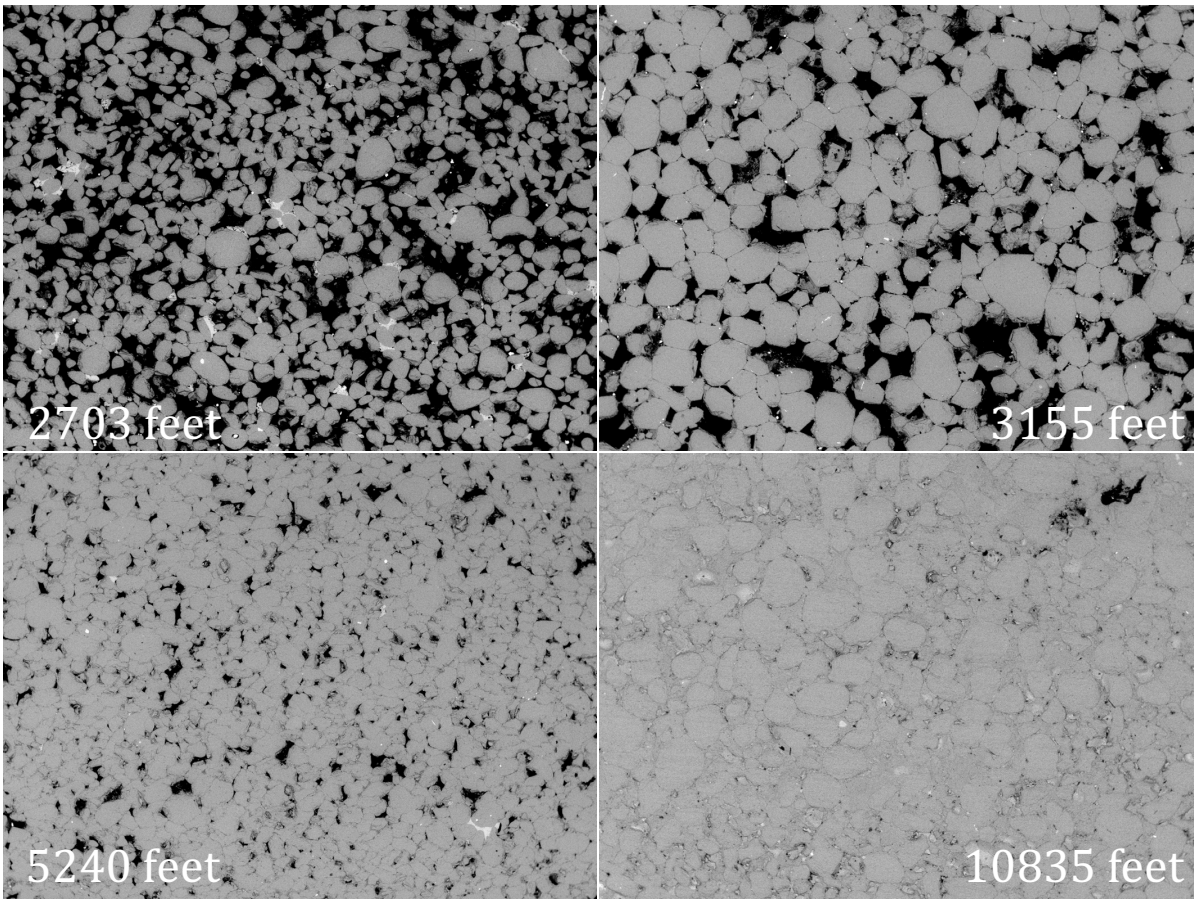

Fig. 1. Backscattered electron images, high- and low-porosity samples versus depth. Each image is 6.35 mm across. All four samples consist largely of quartz grains, although small percentages

of other materials are apparent, and significant dolomite cement is present in the sample from 10835 feet.

leached dolomite cement and detrital grain dissolution. Samples from well C-4831in Marion County, Illinois were moderately well-sorted quartz arenites predominantly composed of well-consolidated, highly compacted, medium to fine, well-rounded to sub-rounded quartz grains. Authigenic quartz, dolomite, and clay were rare. Quartz grains were highly compacted with sutured grain boundaries. Porosity appeared largely a primary framework; however, secondary complete grain dissolution is possible. Porosity was measured from 5.1 to 8.2% in thin section. The relative mineralogical purity of most Illinois samples is consistent with regional mapping of diagenetic mineralogy (Pittman et al., 1997).

Samples from Arenac County, Michigan were moderately sorted quartz arenites composed of moderately consolidated and compacted, fine to coarse, rounded to well-rounded quartz grains. Primary grain-supported pore space was completely cemented by authigenic dolomite sample 10835, but dolomite was completely lacking in the other sample (10816), in which clay was common. Porosity was measured from 0 to 21.5% in a thin section.

Fig. 1 shows BSE images of four of the samples studied. These images clearly indicate the decrease in porosity attributable to compaction and cementation. Most grains are at least moderately well-sorted and rounded. Aa transition occurs with depth from a grain-supported to a more cement-supported structure, although this only dominates one of the two deep samples from the Michigan Basin. Sutured grain boundaries also become more common with depth.

3.2.Analysis of porosity in back-scattered electron imagery

To better quantify porosity at the image scale, the BSE images were first converted to binaries using ImageJ (Abramoff et al., 2004; Rasband, 1997–2016; Schneider et al., 2012;

Anovitz et al., 2013a). Several autothresholding approaches (cf. Anovitz and Cole, 2015) were applied to each image to determine the approximate threshold setting, which was then adjusted as needed. More complex segmentation algorithms (e.g., watershed, edge finding) were not utilized.

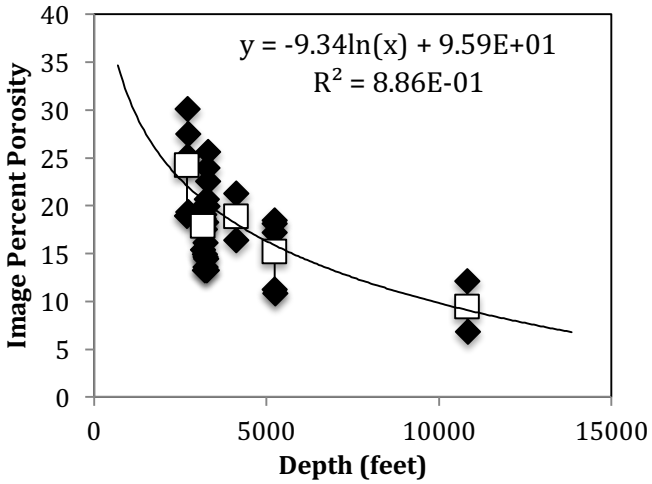

Fig. 2. Image scale porosity as a function of depth for each sample (black diamonds) and the average for each core (open squares).

Fig. 2 shows the image-scale porosity of each of the 36 samples examined as a function of depth, along with the average for all samples from each well. The number of samples from each core differs significantly, but average and one sigma values for percentage of image-scale porosity for each of the cores are as follows: 24.26 ± 4.44 (C-28), 17.91 ± 3.64 (C-13368), 18.88 ± 3.46 (C-228), 15.20 ± 3.81 (C-4831), and 9.48 ± 3.77 (Briggs unit). As expected, average porosity decreases with depth. This change is approximately logarithmic. Although relatively little difference in depth occurs between the samples from each well, considerable variation in porosity is observed at each depth. Thus, trends in these data can easily be lost in this background. To counteract this difficulty, comparisons are made later in this article for the highest and lowest porosity samples from each well. The ~4100-foot (~1250 m) samples are excluded from the low-porosity set because the few samples from well C-228 have image porosities near the high end of the other distributions.

The observed image-scale porosities (Fig. 2) are somewhat higher than those reported by Hoholick et al. (1984). This may reflect sampling bias as the samples obtained by Hoholick et al. (1984) were more widely distributed but generally included fewer samples per core than ours. On

the other hand, the difference may be methodological. Hoholick et al. (1984) determined the percentage of porosity by using point-counting techniques. Magnifications and resolution were not provided. Our results, however, were determined by analysis of SEM images with a pixel edge length of 1.24 μm. It is therefore likely that we analyzed many more points, leading to better statistics. Our ability to resolve and include finer pore sizes may also have been superior, although, grain-boundary pixels add to the uncertainty in image-based analyses.

Analysis of these results suggests that image-scale pore volumes may not be distributed normally. Fig. 3 shows a histogram of the difference between the percentage porosity in each sample and the average value for that core. As can be seen, although the numbers remain small, the histogram suggests that the porosity is bimodal, with one group below and the other at or above the mean. It is unclear whether this is real or a function of the limited sample size and, if it is real, what its origins might be.

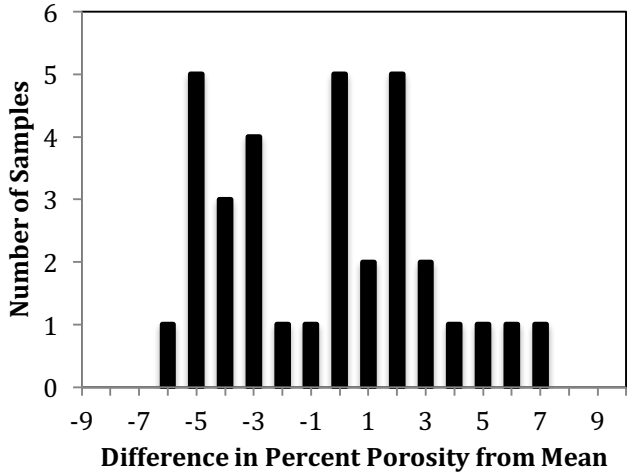

Fig. 3. Histogram of the frequency over all specimens examined from the Illinois and Michigan Basins (southwest Wisconsin samples were not included) of the difference between the image-scale percentage of porosity and the mean porosity for the core from which the sample was obtained. Note the apparent bimodality.

3.3. Combination of small-angle scattering and backscattered electron imagery

As shown by our work to date (Anovitz et al., 2009, 2011, 2013a,b, 2015a,b; Wang et al., 2013), the pore structures of most rock types are inherently multiscalar, with pore sizes ranging from the nanoscale up. The combination of SANS and USANS covers a pore-size range from approximately 7 Å to 15 μm, although the smallest scales are often obscured by background

because of incoherent scattering. This range can be extended to larger scales by using a two-point autocorrelation analysis to combine two- or three-dimensional imaging data with the results of the scattering experiments, covering ranges up to 1 cm or larger (Anovitz et al., 2013a, 2015a; Wang et al., 2013).

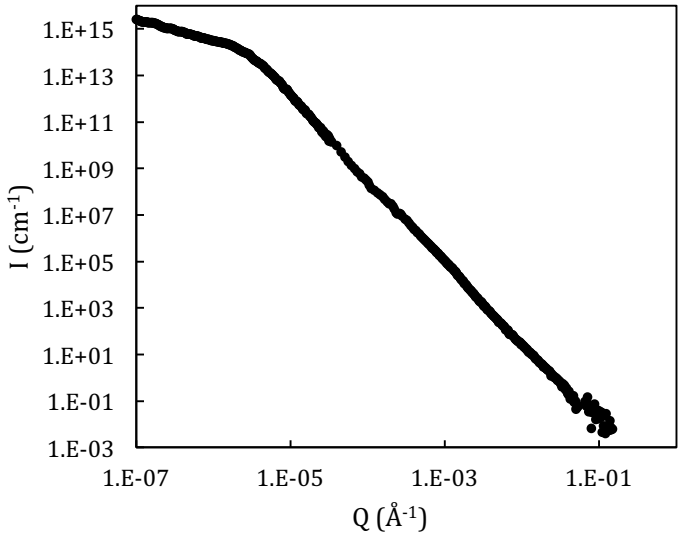

Fig. 4. Example scattering curve C13368 (3276 feet [0.99 km]). Background scattering has been subtracted.

Fig. 4 shows an example of a background-subtracted scattering pattern (sample C13368-3276), as the log of the intensity $I(Q)$ in inverse centimeters as a function of the log of the scattering vector Q ($Å^{-1}$). Although many details are hidden in these data (cf. Anovitz et al., 2013a, 2015a), to a first approximation they can be modeled as two straight lines with an intersection (R) calculated as $2\pi/Q$, a correlation length that represents the largest pore size. For all samples the log-log slope of the

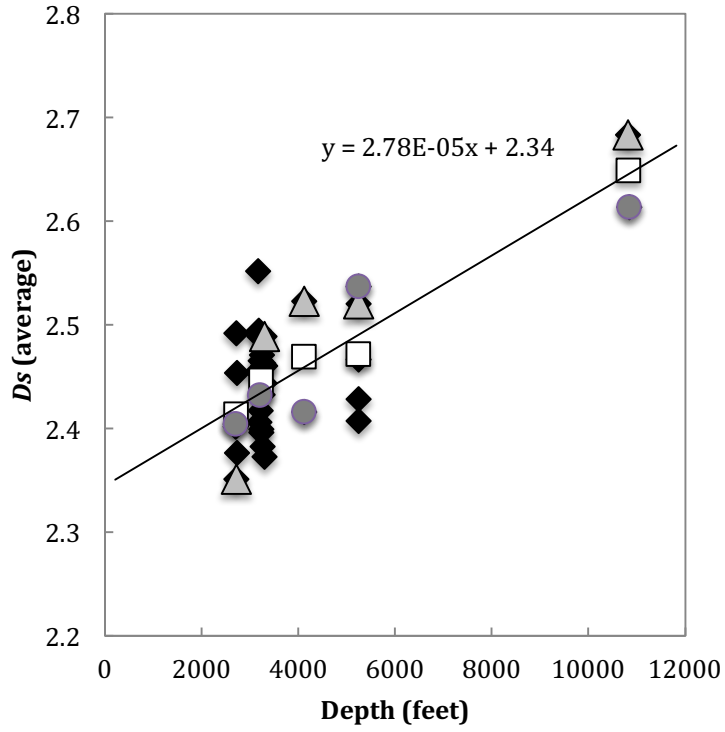

Fig. 5. The surface fractal dimension (D_s), derived from the overall slope of the high-Q portion of the scattering diagram as a function of depth. Averages for each depth are shown as open squares. The highest porosity samples for each depth are

shown as gray triangles, the lowest porosity samples for each depth are shown as gray circles.

curve (n) at higher Q (smaller scales) falls between –3 and –4, reflective of a surface fractal dimension D_s with a value of 6 + n, reflecting both surface roughness and pore-size distribution (Table 2).

Fig. 5 shows the distribution of D_s as a function of depth for the St. Peter Sandstone samples examined. Although the scatter is significant, a clear increase appears as a function of depth, especially for the averages, reflecting a roughening of the grain boundaries from projected values of 2.34 at the surface to 2.67 at 12,000 feet [3.66 km]. This result is consistent with the presence of grain suturing in the more compacted materials and the observation by Kruhl and Nega (1996) that such boundaries are fractal (see also Majumder and Mamtani, 2009; Mamtani and Greiling, 2010). The found, however, that at optically scales D_s decreases with temperature in igneous and metamorphic rocks. This appears inconsistent with the increase in D_s with depth (increasing pressure and temperature) observed in our samples (undergoing diagenesis).

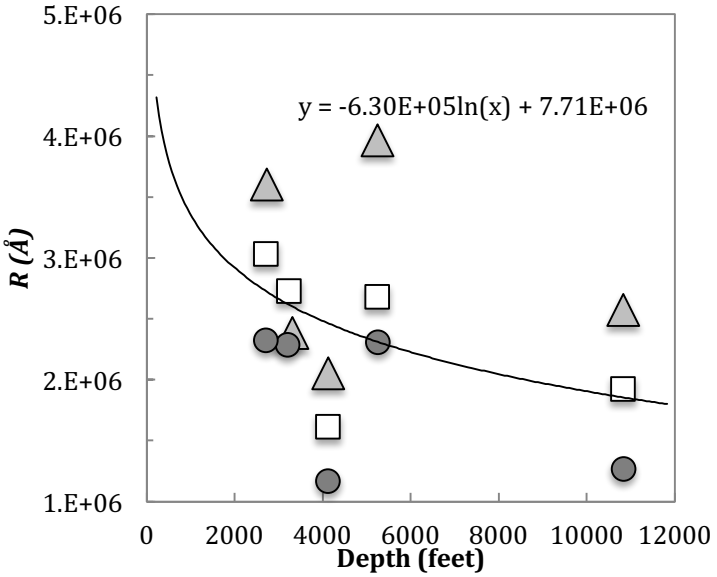

Fig. 6. Correlation length (R) as a function of depth. Averages for each depth are shown as open squares. The highest porosity samples for each depth are shown as gray triangles, and the lowest porosity samples for each depth are shown as gray circles. The trend line is fitted to the average values.

As exemplified by Fig. 4, in most samples a sharp transition can be seen between the low-Q and high-Q parts of the scattering curve. The slope of the scattering curve at low-Q (larger scales) lies between 0 and –1 for all the samples examined. It therefore does not

reflect mass-fractal scattering, for which the slope should be between −2 and −3, but an upper limit to the sizes of the observed pores. Fig. 6 shows changes in this correlation length (R) as a function of depth. As before, significant scatter can be seen at any given depth, but the average values suggest a decrease in R from a value of approximately 300 μm near the surface to approximately 190 μm at 12,000 feet (3.66 km, especially if the limited data set near 4000 feet [1.22 km] is ignored). This result is consistent with the general compaction and cementation of the sample and decrease in the larger pore sizes observed in the SEM imagery (Fig. 1).

The apparent difference between the evolution of our D_s values and those of Kruhl and Nega (1996) may be a factor of scale. Anovitz et al. (2013a, 2015a, and see below), found that, for silcrete formation in St. Peter samples from southwest Wisconsin, D_s decreased at coarser SEM image scales in the same rocks in which it increased at smaller scales in the scattering data. Thus, larger scale images must also be considered for the samples from the Illinois and Michigan Basins.

Fractal dimensions can be obtained from SEM images by direct box-counting monofractal (Block et al., 1991) or multifractal analysis (cf. Anovitz et al., 2013a, 2015a; Anovitz and Cole, 2015). The multifractal approach (Mandelbrot, 1989; Evertsz and Mandelbrot, 1992) includes and is an expansion of the original monofractal description (Mandelbrot, 1977, 1983) that considers nonuniform variations in the overall density of the image. In a multifractal description, self-similarity is scale dependent, and a single exponent is not sufficient to describe the system. Rather, an array of exponents, known as the singularity spectrum, is used. Following our previous work, we have represented the multifractal spectrum using the Rényi dimension $D(q)$, where q, a positive or negative integer, is a deformation parameter that serves to emphasize high- or low-concentration parts of the image (for a fuller description, see Anovitz et al., 2013a, and references therein). Negative values of q emphasize regions of low concentration of the measure (porosity), and

positive values indicate regions of high concentration. Thus, the multifractal spectrum shows how fractal behavior depends on regional variations in pore density. When q is zero, $D(0)$ is the monofractal dimension and, as shown in our previous work (Anovitz et al., 2013a, 2015a), the extent of multifractality can be described simply by showing the difference between $D(0)$ and D at some other value of q.

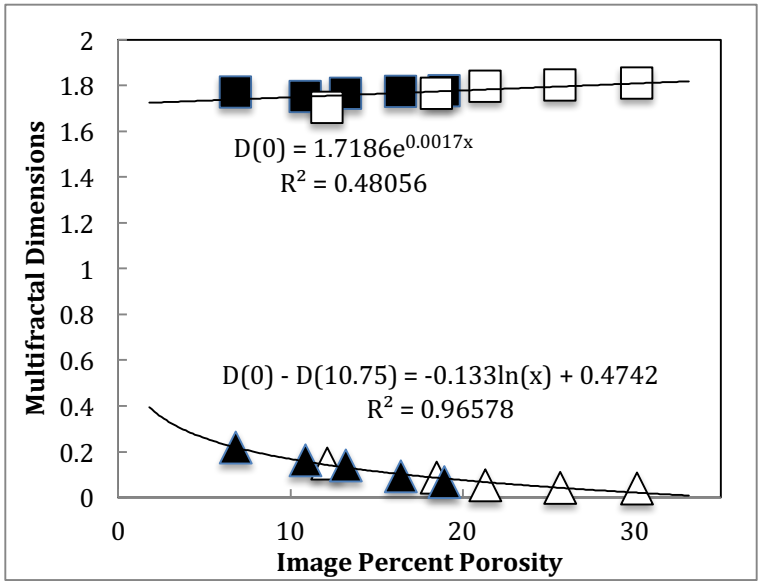

Fig. 7. Changes in the monofractal dimension D(0) (squares) and multifractality D(0) – D(10.75) (triangles) as a function of porosity for both the highest porosity (open symbols) and lowest porosity (filled symbols) samples at each depth. Trends showing both decreasing overall fractality and increasing multifractality with increasing depth are well defined.

Fig. 7 shows the monofractal value [$D(0)$] and the multifractality [$D(0) – D(10.75)$] of the highest and lowest porosity samples from each drill hole as a function of the image-scale porosity. As can be seen, the values for $D(0)$ decrease with decreasing porosity, and therefore with depth. This is opposite the trend observed for the averaged D_s values obtained at smaller scales from the scattering data (Fig. 5), but similar to that observed at larger scales by Kruhl and Nega (1996) with increasing temperature. The multifractality of the pore structures, however, increases with decreasing porosity. Thus, the differences in fractal dimension between the low-concentration and high-concentration parts of the image increase as porosity decreases with depth, but the fractality of the system decreases overall (the pore system becomes smoother).

As discussed by Anovitz et al. (2015a), Cohen (1987) noted that, unlike sintered materials, sedimentary rocks tend to form fractally-rough grain boundaries. He suggested this "antisintering"

behavior was due to reduction of grain or pore free energy by interaction with pore water. Wong et al. (1986) noted that in clean water, roughness is controlled by the competition between thermal fluctuations and surface tension; therefore, a roughening transition temperature, T_r, occurs above which surfaces become rougher with time. In addition, random contamination of atomic-scale growth sites by impurities lowers the T_r, making its occurrence in sedimentary environments more likely (Wong, 1985; Barabási and Stanley, 1995).

The SEM images also allow the lacunarity of the system to be calculated. Lacunarity describes the clustering of features in an image (cf. Anovitz and Cole, 2015). and can also be viewed as a measure of translational homogeneity. It provides a quantification of how isolated each pore, or group of pores, is from others. Analysis of lacunarity as a function of a given geological process therefore provides a measure of whether that process tends to isolate or homogenize the pore structure, a likely indicator of the relationship between changes in porosity and those in permeability.

Fig. 8 shows the relationship of both porosity and multifractality to lacunarity. Lacunarity increases with decreasing porosity (increasing depth) and increasing multifractaility. Although the absolute lacunarity values are relatively small, the relative change with porosity or multifractality is approximately a factor of two. Therefore, at the scale observed in these images (approximately 1.24 μm to 6.35 mm) burial diagenesis tends to make the pore structures smoother but more isolated and more scale dependent. This result is consistent with multifractal and lacunarity behavior observed in the St. Peter Sandstone in southwest Wisconsin (Anovitz et al., 2013a), where silcrete precipitation with little or no compaction is the primary cause of changes in porosity. Whether the effects of dolomite precipitation are the same as those of quartz overgrowth, however, remains unknown.

This result is also consistent with our observations regarding the experimental precipitation of quartz in samples of St. Peter Sandstone (Anovitz et al., 2015a).

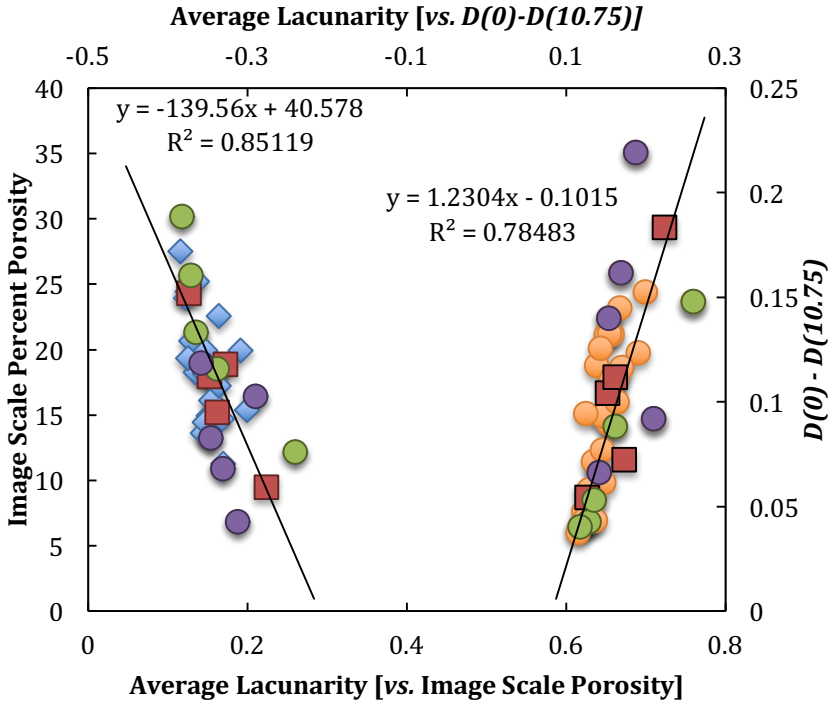

Fig. 8. Relationships between average lacunarity, image-scale porosity (blue diamonds) and multifractality expressed as *D(0) – D(10.75)* (orange circles). Values for the highest porosity (green circles), lowest porosity (purple circles), and mean values (red squares) for each depth are highlighted.

Although the multifractalities are similar, the absolute change in *D(0)* is somewhat larger for the silcretes than for the basinal sandstones over a similar range of porosities; thus, *D(0)* values for low-porosity samples tend to be smaller for silcretes than for basinal sandstones. The same is true at finer scales (Fig. 5) in which, as depth increases and average porosity decreases, the surface fractal dimension D_s increases. As noted above, this is in contrast to what is observed at larger scales. The D_s values observed in the silcretes (2.19–2.56) are also smaller than those in the basinal sandstones (2.35–2.68), although the extent of the latter is primarily a function of samples from the Briggs Unit core. A reasonable positive correlation also exists between the lacunarity and *D(0) – D(10.75)* (Fig. 8), suggesting that, to some extent, lacunarity and multifractality are recording similar phenomena. It is therefore clear that several qualitative similarities exist between changes in the pore structure due to simple cementation and those observed with burial-related processes. It is uncertain, however, whether this result implies that the overall effects of cementation and compaction on the pore structures of sandstone are

similar, or whether the current pore structures of the samples from the Illinois and Michigan Basins are dominated by precipitative or dissolution–reprecipitation processes that are qualitatively similar to those observed during silcrete formation.

3.4 Detailed (U)SANS Analysis

Despite the apparent regularity of the slope and *R* versus depth data presented in Figs. 5 and 6, as we have pointed out previously (Anovitz et al., 2013a, 2015a), the data do not, in detail, consist of a simple, straight line reflecting a pure surface fractal over a wide range of scattering vectors and intensities. Instead, the scattering curves consist of a series of subtle steps, reflecting individual pore-scale distributions that may, or may not, be overlain on a fractal background. This is best seen by replotting the data in terms of Q^4I as a function of Q, which effectively flattens a scattering curve with a slope of –4 in log Q versus log $I(Q)$ space (the slope expected for scattering from a smooth surface), allowing the curve to be seen in greater detail by expanding the vertical axis of the graph. Figs.9 and 10 show this "Porod transform" of the background- subtracted data for the lowest porosity samples at four depths, and the highest

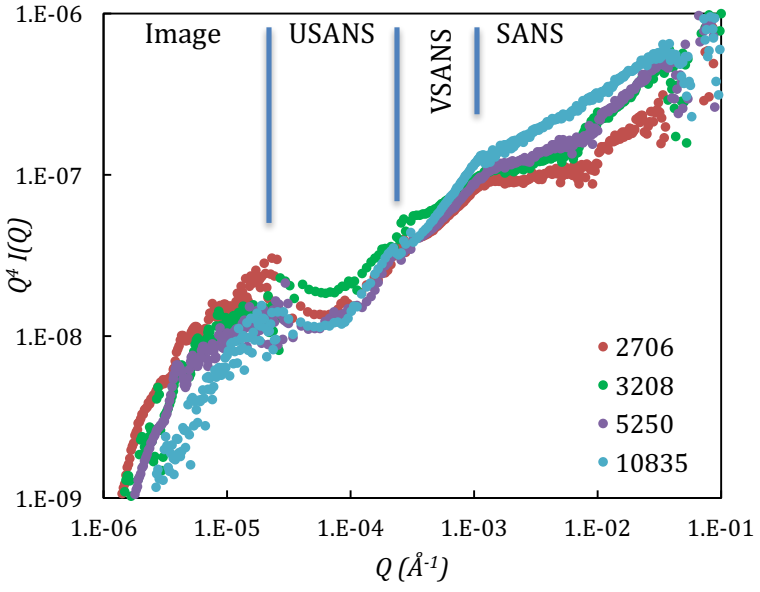

Fig. 9. Porod transformed scattering curves with calculated additions from backscattered electron images for the four lowest porosity samples at each depth. Approximate ranges of data for each instrument are shown, although some overlap exists. SANS, VSANS, and USANS refer to small-, very-small-, and ultra-small-angle neutron scattering.

porosity samples at five. The data have been slightly truncated

primarily to show the higher-Q data, although the intersection between those and the low-Q results is also included.

Several features are apparent in Figs. 9 and 10. Again, the high-Q portion of the data cannot be completely described by a single slope defining a single D_s value, but is composed of a series of steps or peaks, often at similar Q values. Anovitz et al. (2013a) considered and disproved the possibility that these steps reflect the intersections between detector positions in the SANS instrument. That conclusion is further supported in the present data set by the results near $Q = 10^{-3}$ Å^{-1}, which were obtained on the VSANS instrument (not utilized by Anovitz et al., 2013a) at a single detector position, and near $Q = 10^{-4}$ Å^{-1}, which were obtained on a USANS instrument, also at a single detector position. Both instruments show similar steps.

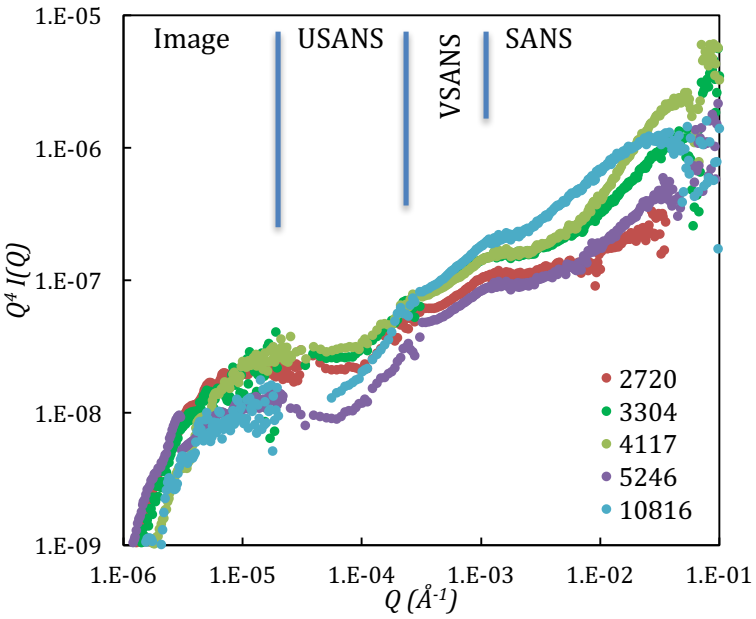

Fig. 10. Porod transformed scattering curves with calculated additions from backscattered electron images for the five highest porosity samples at each depth. SANS, VSANS, and USANS refer to small-, very-small-, and ultra-small-angle neutron scattering.

The data also show a distinct pattern of changes as a function of depth. At larger scales (near $Q = 10^{-5}$ Å^{-1}), the intensity of the scattering curve, and therefore the porosity of the sample in approximately that size range, decreases with depth. This result is as expected and reflects the loss of the larger pores with depth due to compaction and cementation. At smaller scales (near $Q = 10^{-2}$ Å^{-1}), however, the deepest samples have the largest intensity, implying increased nanoscale porosity with increasing depth. This pattern is, however,

clearer for the lowest porosity samples at each depth (Fig. 9) than for those with the greatest image-scale porosity (Fig. 10).

Figs. 11 and 12 show calculated pore volume distributions for the lowest and highest porosity samples from each drill core, respectively. These distributions were calculated by using the total nonnegative least squares approach coded in the Irena plugin for IGOR (Ilavsky and Jemian, 2009). Each was run 10 times to estimate uncertainties, assuming, in each case, spherical pores and that only quartz and pores were present. Data for 04Wi17bPRL and 05Wi02, the lowest and highest porosity samples from the St. Peter Sandstone at the surface in southwest Wisconsin (Anovitz et al., 2013a), have been included for comparison, although the total porosity for 04Wi17bPRL is much lower than expected from the trend shown in Fig. 2 because of the large amount of silcrete cement it contains.

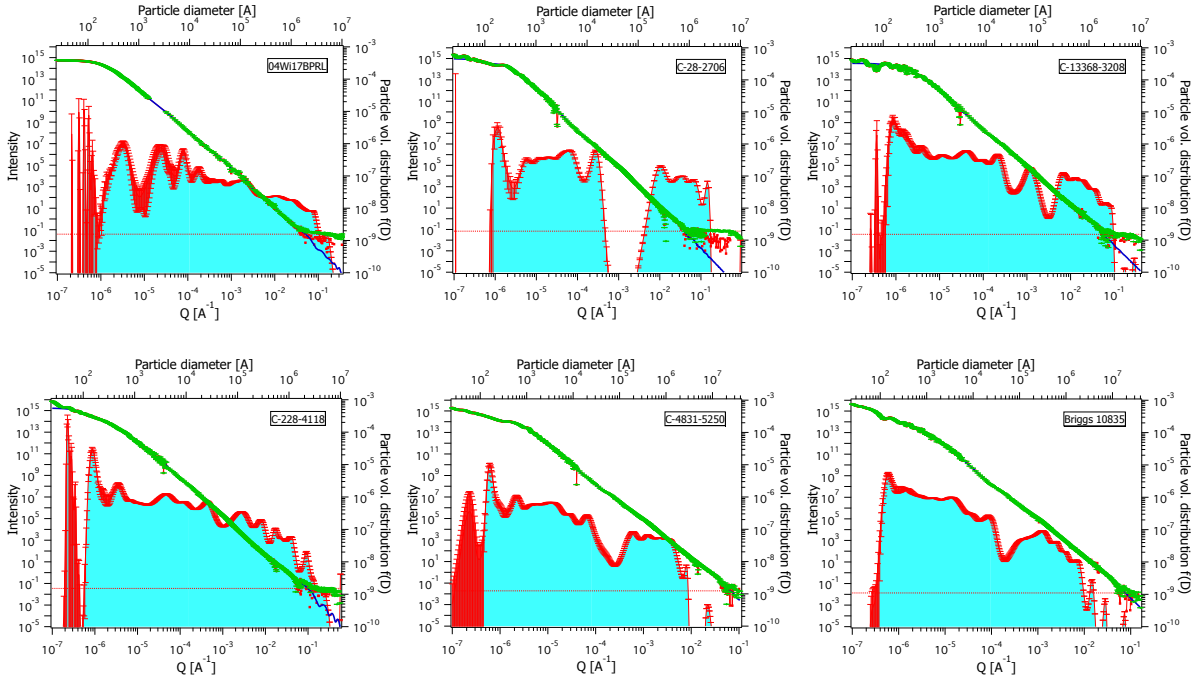

Fig. 11. Pore volume distributions, calculated using the total nonnegative least squares approach (Merrit and Zhang, 2004; Ilavsky and Jemian, 2009), assuming spherical pores for the samples with the lowest pore volume in each core. Calculations for sample 04Wi17bPRL (Anovitz et al., 2013a), the lowest porosity sample from the surface-exposed St. Peter Sandstone in southwest Wisconsin have been included for comparison. Red points with green error bars indicate measured data. The blue line is a fitted curve. The light blue area with red error bars indicates the calculated pore distribution. The dashed red line is the background.

It is clear from all pore distributions shown that, rather than consisting of a continuous distribution of pore sizes, the porosity distribution for each sample is dominated by a series of log-normal-like distributions, the apparent intensity of which is somewhat visually suppressed in Figs. 11 and 12 by the logarithmic intensity scale. The calculated pore volume distributions are, however, somewhat dependent on the approach used for the calculation and on the assumed geometry of the scatterers. The latter is illustrated in Fig. 12, which shows the total nonnegative least squares solution for sample 2720 for spheroids with aspect ratios of 2 (prolate), 1, and 0.5 (oblate). Changing from a prolate to an oblate spheroid tends to narrow the individual pore distributions, although the total pore volume of necessity remains constant.

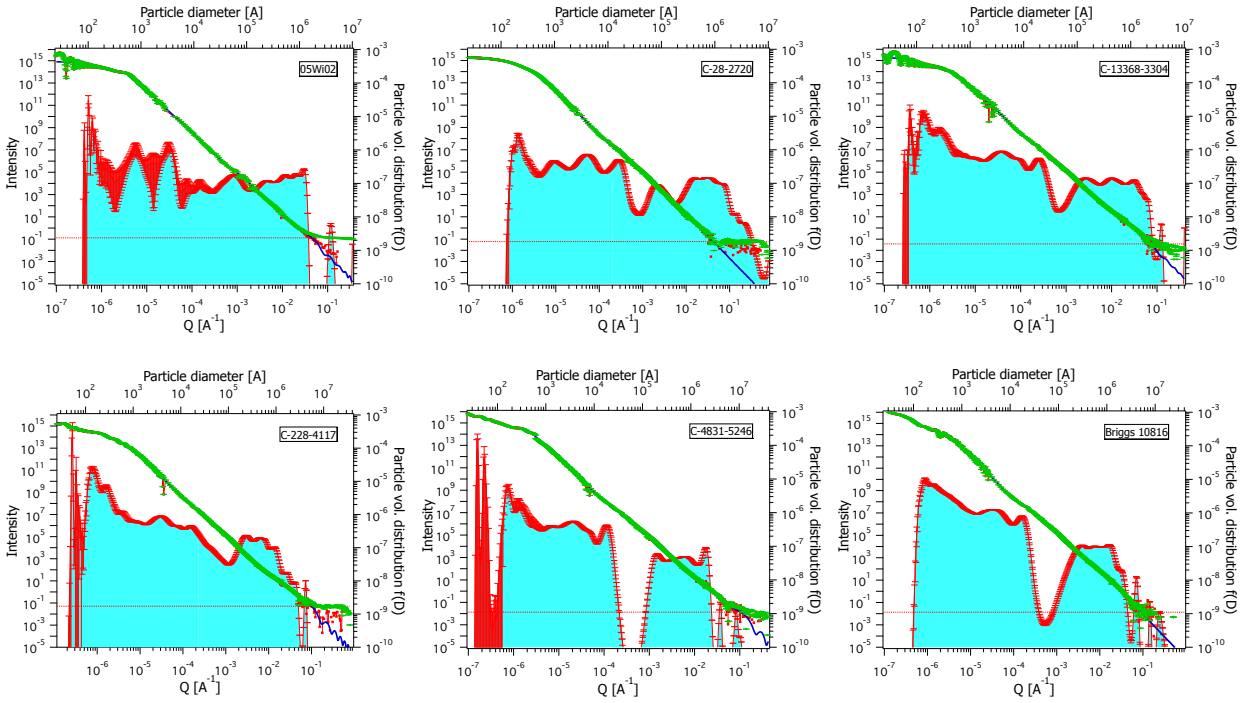

Fig. 12. Pore volume distributions, calculated using the total nonnegative least squares approach (Merrit and Zhang, 2004; Ilavsky and Jemian, 2009) assuming spherical pores, for the samples with the highest pore volume in each core. Calculations for sample 05Wi02 (Anovitz et al., 2013a), the highest porosity sample from the surface-exposed St. Peter Sandstone in southwest Wisconsin, have been included for comparison. Red points with green error bars indicate measured data. The blue line indicates a fitted curve. The light blue area with red error bars indicates the calculated pore distribution. The dashed red line indicates the background.

Although the intensities of the larger pore diameter distributions appear small, because the total volume of each distribution is the integral of each, the volumes of these distributions are significantly larger than those representing smaller pore sizes. In addition, the uncertainties of many of the smallest pore distributions are relatively large. This result is caused by the proximity in both intensity and Q of the scattering data at these scales to the incoherent background.

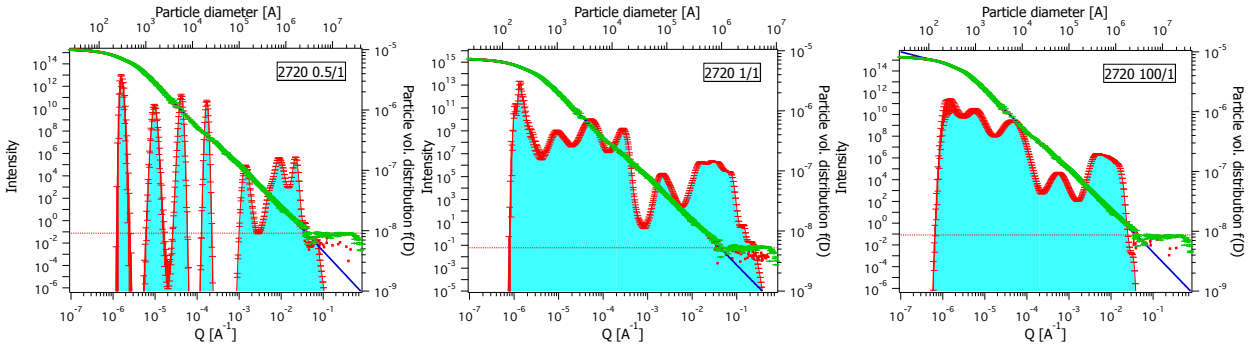

Fig. 13. Pore volume distributions and scattering curves for sample 2720 calculated for spherical aspect ratios of 100 (prolate), 1, and 0.5 (oblate). Note that in all cases, the pore structure consists of a series of log-normal-like distributions and that the sizes of each distribution are similar for all three solutions.

Many of the calculated pore-size distributions in Figs. 11 and 12 show a minimum near 4 × 10^4 Å (4 μm), or $Q \sim 1.6 \times 10^{-4}$. This is well within the range of the USANS data in the area where Q^4I is dropping rapidly in Figs. 9 and 10. This gap is not, however, present in the low-pressure samples from southwest Wisconsin. This result suggests that, within the uncertainties in the total nonnegative least squares approach, this is a real break in the pore sizes, not an analytical artifact, and that the pore-size distributions might be separable into two generalized groups of larger and smaller pores, perhaps implying a different genetic origin. The larger of these two distribution groups is, in most cases, composed of three to four relatively regularly spaced individual distributions, the volume of which decreases with increasing burial depth. The opposite

appears to occur for the smaller pore distributions. This result is consistent with changes in the scattering curve intensities shown in Figs. 9 and 10.

4. DISCUSSION AND CONCLUSIONS

From the data summarized above, it is clear that there are significant changes in the pore structure of the St. Peter Sandstone with depth in the Illinois and Michigan Basins. As discussed by Stack (2015), however, a primary question is how overall porosity changes as a function of pore size distributions.

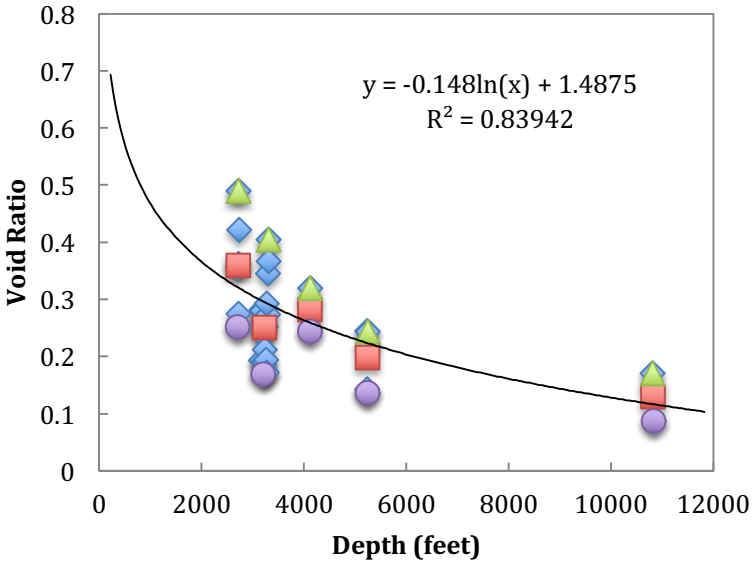

Fig. 14. Change in the void ratio [ϕ(pore)/ϕ(rock)] as a function of depth.

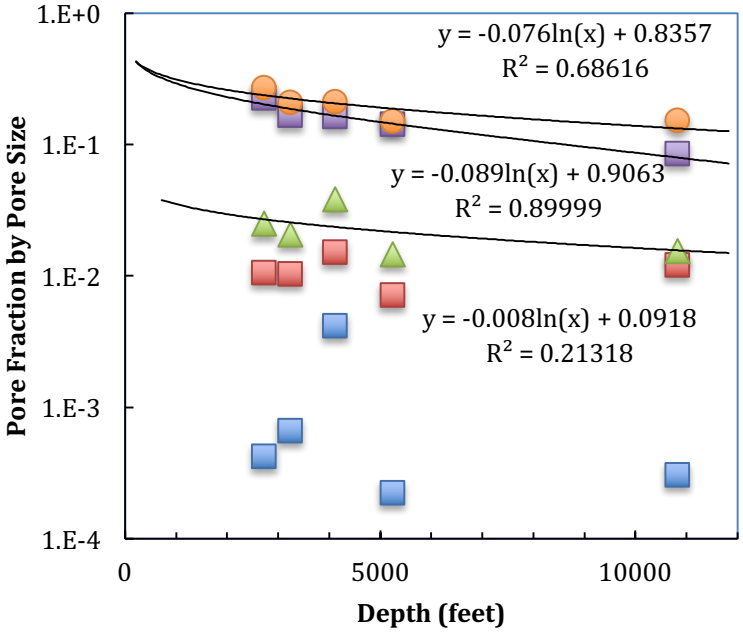

Fig. 15. Average pore fractions as a function of depth for various pore-size ranges: log[r(Å)] > 1.4 (orange circles), log[r(Å)] > 5 (purple squares), 5 > log[r(Å)] > 4 (green triangles), 4 > log[r(Å)] > 1.4 (red squares), log[r(Å)] < 1.4 (blue squares).

Available data suggest that different geological processes can have significantly different effects on pore-size distributions. For instance, as discussed above, silcrete formation in the St. Peter Sandstone in southwest Wisconsin tended to fill larger pores first

(Anovitz et al., 2013a, 2015a). By contrast, high-temperature, low-pressure metamorphism in the Hatrurim Formation in Israel (Wang et al., 2013) had the opposite effect: smaller pores were filled first. Figs. 14–16 show changes in the overall void ratio [ϕ(pore)/ϕ(rock), image plus scattering] and in the absolute and normalized pore-size fractions as a function of depth. These values are summarized in Table 2. The total pore volume decreases logarithmically as a function of depth, as does the image-scale porosity (Fig. 2). This result is consistent with the logarithmic relation first proposed by Terzaghi (1923; see also Athy, 1930; Biot, 1941; Skempton, 1944; Parasnis, 1960; Fowler and Yang, 1998; Bahr et al., 2001). Although more recent work has included the effects of overpressures (Rubey and Hubbert, 1959; Smith, 1971), elastoplastic behavior (Shi and Wang, 1986; Audet and Fowler, 1992; Schneider et al., 1993, 1996), and three-dimensional effects (Pouya et al., 1998), this correspondence suggests that most of the volume change observed is due to compaction. This logarithmic behavior is not, however, consistent across all pore scales. As can be seen in Fig. 15,

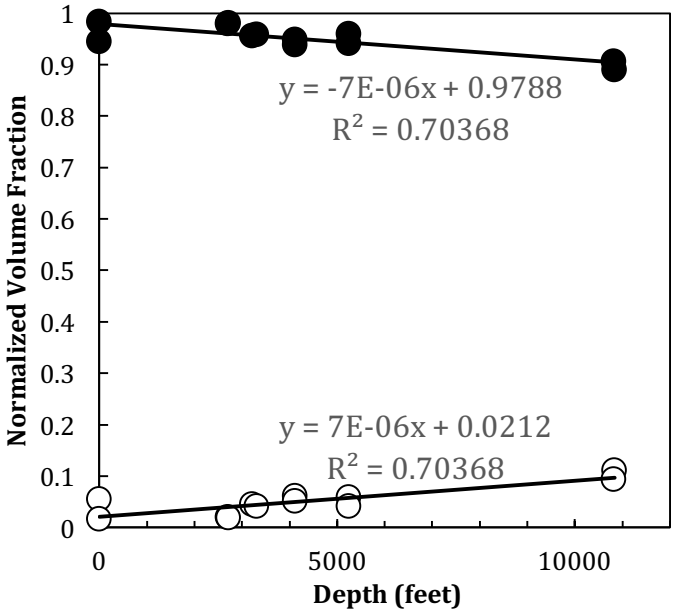

Fig. 16. Volume fraction normalized to 100% total. Pores with radii greater than 10^4 Å are shown as solid circles, and pores with radii smaller than 10^4 Å are shown as open circles.

most of the absolute change in volume occurs through the loss of the larger pores. Little or no change occurs in the *absolute* volume of the smallest pores (log[r(Å)] < 4), although the fraction of intermediate-sized pores (5 > log[r(Å)] > 4) does appear to decrease (weakly) with depth. Nonetheless, as a percentage of the total porosity (Fig. 16), the percentage of smaller pores

($\log[r(\text{Å})] < 10^4$ Å) increases significantly. To the extent that these changes can be determined from our data, they do not appear to be logarithmic, but rather nearly linear as a function of depth.

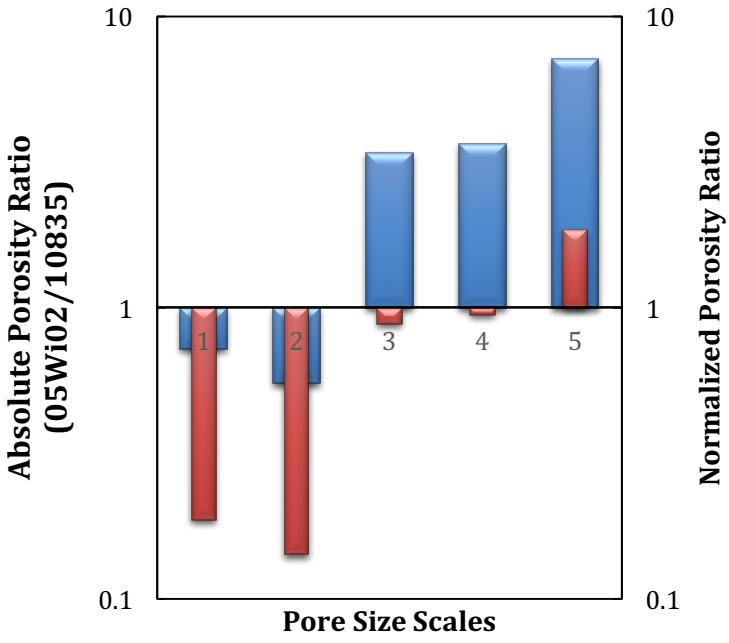

Fig. 17. Ratio of pore volume fractions (absolute, red; normalized, blue) between the most porous sample (05Wi02) and the least porous sample (10835). Pore volumes were obtained from the total nonnegative least squares calculations shown in Figs. 11 and 12. (1) $<10^3$ Å, (2) 10^3–10^4 Å, (3) 10^4–10^5 Å, (4) 10^5–10^6 Å, (5) $>10^6$ Å.

The relative changes in pore volumes at different scales can be seen more clearly by plotting the ratio of the pore volumes (either normalized or not) at each scale of the most porous sample (05Wi02 from southwest Wisconsin) to those of the least porous sample (10835 from the Briggs Unit well in the Michigan Basin). Increasing depth and decreasing overall porosity decreases the absolute porosity only at scales larger than 10^6 Å; when normalized to 100%, all fractions at scales larger than 10^4 Å increase, although only a slight decrease occurs in the absolute porosity between 10^4 and 10^6 Å, in both the normalized and the absolute cases, the fractions of pores with radii below 10^4 Å increase with depth. Although changes in the absolute pore fraction are small, this ratio increases significantly, by a factor of nearly seven. This result implies a large increase in the number of such small pores. Assuming this porosity is connected (cf. Hu et al., 2012) or that these pores represent pore throats, or both, this result may have a dramatic impact on

the available reactive surface area in the rock. These results are consistent with the qualitative conclusions drawn above from Figs. 9 and 10.

The surface area per unit volume is a critical variable of the pore structure because of the limits it places on reactivity, although the total, accessible, and reactive surface areas are not necessarily identical. The effects of compaction and cement overgrowth on the surface area of a grain can be estimated by considering some simple geometry. If we assume that compaction merely reforms grain shapes to fill space, then its effects on the surface area can be estimated by comparing the surface area of a sphere to that of a space-filling regular dodecahedron of the same volume. A sphere with a volume of 1 cm^3 has a surface area of 4.84 cm^2. If that same sphere is re-formed into a regular dodecahedron with the same volume, the surface area increases to 5.31 cm^2, an increase of 9.82%. Conversely, overgrowth formation can be modeled as the formation of a regular dodecahedron around an inscribed sphere (one that is tangent to each of the faces of the dodecahedron). A sphere with a volume of 1 cm^3 has a radius of 0.62035 cm. The edge length of the dodecahedron in which this sphere is inscribed is 0.5571 cm, which yields a volume of 1.325 cm^3 and a surface area of 6.41 cm^2, a 32.4% increase in surface area.

Similarly, we can estimate the effects of flattening or elongation of pores on surface area. Fig. 18 shows the surface area of a spheroid of rotation as a function of its axial ratio under two conditions: constant volume and constant diameter (of the circular section). For a constant volume spheroid with a volume of 1 cm^3, the surface areas are 5.30 cm^2 for a 0.5:1 oblate spheroid, 4.84 cm^2 for a sphere, 6.43 cm^2 for a 2:1 prolate spheroid, and 33.07 cm^2 for a 100:1 prolate spheroid, relative changes of –8.7, 32.9, and 414.3%, respectively. For a constant diameter spheroid with a diameter of 1 cm, the surface areas are 2.17 cm^2 for a 0.5:1 oblate spheroid, 3.14 cm^2 for a sphere,

6.63 cm^2 for a 2:1 prolate spheroid, and 462.84 cm^2 for a 100:1 prolate spheroid, for relative increases of 44.7, 111.1, and 6881.0%, respectively.

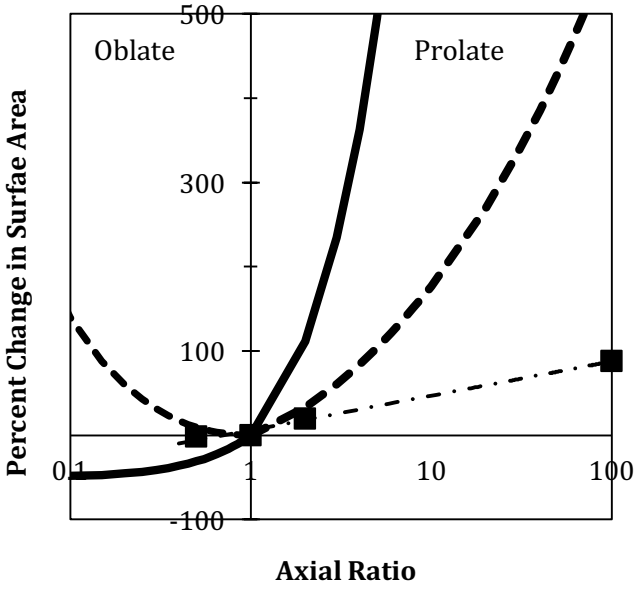

Fig. 18. Percentage change in surface area relative to a sphere for a spheroid of rotation for either constant volume (dashed line), or a constant diameter circular section (solid line). An oblate spheroid approximates a grain boundary between crystal faces, and a prolate spheroid approximates a grain edge boundary. The dashed-dotted line connects points calculated for sample 2720.

Pore distributions calculated using the total nonnegative least squares approach allow us to make similar calculations for the samples of St. Peter Sandstone. As shown in Fig. 13, the more oblate the pores, the more separated and narrow the estimated pore distributions become, which tends to yield smaller surface areas. These calculations were made for a constant total pore volume, although the number of pores at any given size is not necessarily constant. Surface areas estimated for sample 2720 (Fig. 18) are 1734 cm^2/cm^3 for a 0.5:1 oblate spheroid, 1796 cm^2/cm^3 for spherical pores, 2118 cm^2/cm^3 for a 2:1 prolate spheroid, and 3326 cm^2/cm^3 for a 100:1 prolate spheroid, relative increases of 3.6, 17.9, and 57.0%, respectively. For sample 10835, the lowest porosity sample, the relative surface areas are 3452 cm^2/cm^3 for a 0.5:1 oblate spheroid, 3893 cm^2/cm^3 for spherical pores, 4328 cm^2/cm^3 for a 2:1 prolate spheroid, and 7124 cm^2/cm^3 for a 100:1 prolate spheroid, for relative increases of 12.8, 11.8, and 64.6%, respectively. Even for oblate spheroids, the surface areas for the natural samples calculated using this approach are quite high. This result reflects the larger numbers of very small pores modeled

in each sample. The extent to which this represents accessible or reactive porosity, however, remains uncertain.

When the results of the fits to our scattering data are compared with Fig. 18 on the prolate side, model changes for both constant volume and constant diameter compression are larger than observed. On the oblate side, however, the observed change lies between the two alternatives and decreases with a decreasing axial ratio. This suggests that the majority of pores composing the measured surface area (i.e., the smaller pores) are slit- or discus-like and more consistent with interfacial spaces than with channel-like pores along intergrain triple junctions. Lee et al. (1991) suggested, following Toramaru and Fujii (1986) and Watson and Brenan (1987; see also Bulau, et al., 1979; Waff and Bulau, 1979; von Bargen and Waff, 1986), that for wetting angles less than 60 degrees,

> "fluid-filled triple junction channels interconnect at four-grain junction tetrahedra having concave faces. Grain boundaries are nonwetted; any fluid present there occurs as discus-shaped fluid inclusions" (p. 10,025), whereas for larger wetting angles, "the bulk of the fluid is isolated at four-grain junction tetrahedra having flat to convex faces. Fluid present in triple junctions is segregated into discrete, football-shaped fluid inclusions. Similarly, in grain boundaries, fluid is segregated into discus-shaped fluid inclusions" (p. 10,025).

Thus, our results suggest that these "discus-shaped fluid inclusions" form a significant portion of the overall pore structure. Laporte and Watson (1991) obtained similar experimental results, including evidence of discus-shaped pores on grain faces. In SEM images, many of these grain face pores appear to be isolated, what Hiraga et al. (2001) called a "necklace microstructure" when observed by transmission electron microscopy.

Such grain boundary pores may or may not remain connected to the rest of the pore system, but open connectivity may occur at the nanoscale (see Royne and Jamtveit, 2015). For instance, Kruhl et al. (2013) found that quartz grain boundaries in contact and regional metamorphic rocks were open on the nanometer scale. It is unclear, however, whether these surfaces are wetted (see Farver and Yund, 1992, 1995). In addition, Takei (2010) found that under nonhydrostatic stresses, additional grain boundary wetting occurred on surfaces normal to the maximum tensile stress direction (σ_3; see also Daines and Kohlstedt, 1997; Zimmerman et al., 1999, Takei and Katz, 2013). Similar complexities also have been found on grain surfaces in quartz mylonites (Mancktelow et al., 1998). These conclusions are clearly consistent with the observation above that oblate or discus-shaped pores are dominant when the overall surface area is considered. The extent to which such porosity is connected to, or isolated from the remainder will, therefore, have a significant effect on transport and reactivity.

Fig. 19 (triangles) shows the changes in surface area as a function of depth calculated from the pore volume distributions. As the above analysis suggests, the pores controlling the total surface area are largely oblate, whether connected or not. Because variations in axial ratio make relatively small differences in the surface area calculated for oblate systems, we can approximate this variation by calculating the surface area for spherical pores. The results show a general increase in surface area with depth. The surface area calculated in this manner for sample 10835 is approximately a factor of two larger than that of sample 2720 (ratios range from 1.99 to 2.17, depending on the axial ratio). In addition, a large percentage of this surface area is from the smallest pores. For sample 2702, 44% of the surface area is on pores with diameters less than 1000 Å, and for sample 10835, 67% is from pores of this size range. The surface areas for some of the 3000- and 4000-foot-depth (0.91- and 1.22-km-depth) samples increased by significantly larger

ratios (up to about 5.5), implying that a process other than compaction was involved. This result may be explained by the fact that the 4118-foot (1.26-km) sample contained abundant fine-grained dolomite cement with rare, later, coarser euhedral dolomite rhombohedra, which appears to have yielded an *R* value well below the overall trend (Fig. 6). The relatively large value for sample 10816 (Table 2) may be due to its significant clay content.

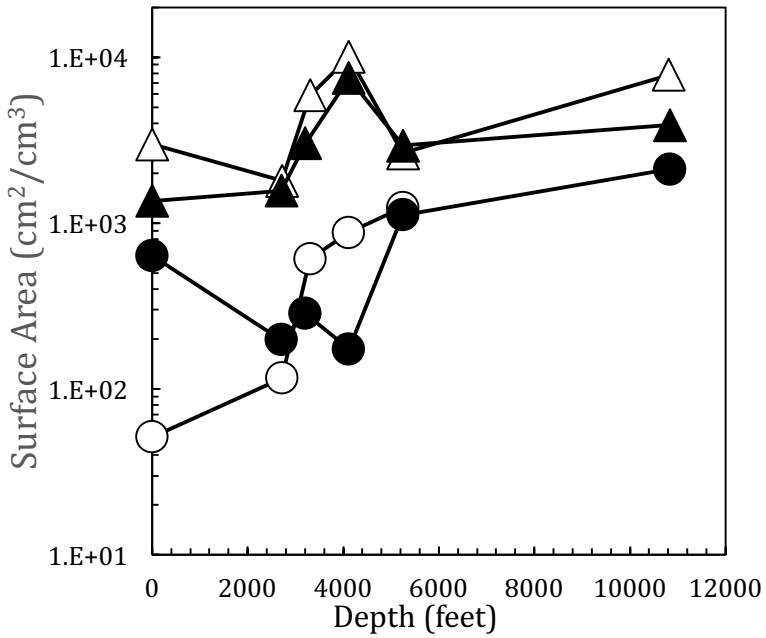

Fig. 19. Surface areas for the high- (open symbols) and low-porosity (filled symbols) samples from each core. Triangles show the surface area calculated from the spherical pore-size distributions shown in Figs. 11 and 12. Circles show the relative surface area to volume ratio calculated from D_s. Data are not shown for sample Briggs-10816, which has a much higher surface area, probably because of its clay content.

The proportional increases in surface area calculated from the pore volume distributions (Fig. 19) are significantly larger than those predicted for either compaction or cement overgrowth precipitation. The pore shape assumed does not, however, account for the observed increase in the surface fractal dimension (Fig. 5), which suggests a roughening of the pore–grain interface, and therefore predicts an increase in the surface area larger than that for polyhedral compression or overgrowth formation. Where spheroidal pore shapes are assumed, such roughening is reflected by an increase in the number of smaller diameter pores. This may be related to the various dissolution events experienced by these samples (Hoholick et al., 1984, Fishman 1997, Freiburg et al., 2016).

Following Allen (1991) and Anovitz et al. (2009), surface areas can be calculated from the surface fractal dimension D_s as

$$\left(\frac{S}{V}\right) = \left(\frac{S}{V}\right)_0 \left(\frac{r}{d_0}\right)^{2-D_S}, \quad (1)$$

where $(S/V)_0$ is the surface area-to-volume ratio for a smooth particle, r is the fractal "ruler" length, d_0 is the correlation length representing the upper limit of surface fractal behavior, and D_s is the surface fractal dimension. Thus, if $D_s = 2$, the particle is smooth and (S/V) is equal to $(S/V)_0$, and if $D_s > 2$, (S/V) is greater than $(S/V)_0$. It should be noted, however, that these surface areas represent only those surfaces that scatter neutrons. Tight quartz/quartz grain boundaries, for instance, will not be represented because no scattering length contrast exists. Because the rocks consist largely of quartz and are essentially isotropic, a value of 4.834 Å, calculated as the cube root of the quartz unit-cell volume (113.0 $Å^3$), was selected for the ruler length. This is, however, an arbitrary selection. The larger the value chosen for r, the smaller the values of $(S/V)/(S/V)_0$. In addition, because r is raised to the 2-D_s power, the closer the value of r becomes to those of d_0, the smaller the effect of changes in D_s on $(S/V)/(S/V)_0$. For these calculations, the values of R shown in Fig. 6 and Table 2 were used for d_0. These are larger than the values for 2l, the surface fractal/mass fractal boundary (cf. Wang et al., 2013), because no such boundary was observed in our data.

The results of this calculation are shown as circles in Fig. 19. Data are not shown for sample Briggs-10816, which has a much higher $(S/V)/(S/V)_0$ value, probably because of its clay content. The $(S/V)/(S/V)_0$ values for both the lowest and highest porosity samples increase significantly between about 3000 and 5000 feet (910 and 1520 m), although this is at somewhat deeper depths for the lower porosity samples, which may be due to dolomite cement in sample 4118. This correlates to porosities of approximately 0.1 for the lowest porosity samples and 0.3 for the highest, and correlate with a change in the porosity type. Hoholick et al. (1984) noted that primary porosity

is dominant at depths to 4000 feet (1220 m), but secondary porosity becomes dominant for deeper samples. The single available data point from samples below 6000 feet (1830 m) from Briggs-10835 suggests that this increase continues with increasing depth. This result reflects increases in the D_s values with depth as well, and probably the increasing presence of sutured grain boundaries, and possibly multiple generations of dolomite cementation and other fractal roughening. It must be remembered, however, that D_s in this case is an average over the whole scale or intensity range of the scattering data and does not necessarily reflect the multiple log-normal-like pore distributions seen when the data are examined in detail.

Contrasting the data obtained in this study with those from the St. Peter in southwestern Wisconsin (Anovitz et al., 2013a), which has never been buried to any significant depth, allows a comparison to be made between the effects of overgrowth formation in samples that have not been deeply buried and burial diagenesis on the pore structure of a sandstone. As noted above, the two data sets show similar results in terms of the evolution of the pore-size distribution, fractal and multifractal behavior, and lacunarity with depth. In addition, in both datasets the pore distribution is noncontinuous. Anovitz et al. (2013a, 2015a) suggested that the multiple distributions observed in the St. Peter Sandstones were due to packing of polydispersed particles following a nondeterministic form of an Apollonian gasket, with smaller particles packing into the spaces between the larger ones. A similar model has been suggested for soils (Hillel, 1980) and dense granular systems (Anishchik and Medvedev, 1995). In fact, as noted by Desmond and Weeks (2014), such packings have attracted a great deal of interest because of their applications to a wider variety of materials and processes, including living cells, granular media, emulsions or colloids, glasses, amorphous solids, jamming, and suspension viscosity, and a large number of articles have been published on the topic. Sohn and Moreland (1968) investigated the effect of particle-size

distributions on the packing efficiency of natural sands, in part using Ottawa Sand, mined in Ottawa, Illinois, from the St. Peter Sandstone, as a starting material. They found that for both Gaussian and log-normal distributions packing density increased with the polydispersivity of the sand distribution. Such a result is likely due to packing of smaller grains between larger ones, and thus will generate a range of smaller pore sizes, which will also be controlled by grain size, sorting and shape, both initially and as the rock evolves (Beard and Weyl, 1973). In fact, Amirjanov and Sobolev (2006, 2012) showed that pore fraction is an inverse power-law function of the number of particles for both Apollonian and random Apollonian packings. This is also true as a function of the number of grains with a radius larger than some cutoff value (ζ; Herrmann et al., 1990; Anishchik and Medvedev, 1995). In neither case, however, was the effect on the pore-size distribution considered, nor is it immediately clear whether such scalings would give rise to a stepped pore-size function. In part, this is because the definition of pore sizes depends on pore shape, which is not spherical for packings of spherical particles. For the St. Peter, this analysis is made more uncertain by the relatively high sorting of the sand, which reduces the number of grains able to fit into the smaller interparticle spaces, although Fig. 1 suggests this may be less true for the deeper material from the Michigan Basin.

The changes in pore-size distributions observed in the St. Peter Sandstone are also consistent with other predictions from soil research (cf. Nimmo, 2004, 2013), which suggest mechanical compression can decrease the size of, or even close macropores. The number of smaller pores may increase because of the size reduction of the larger, or decrease because of disaggregation, reducing the number of intra-aggregate pores, although the latter is less likely in a clean sandstone like the St. Peter. For example, in an experimental study of soil compression, Kutílek et al. (2006) found a decrease in larger scale porosity (>10 μm) and, in some cases, an

increase in the fraction of smaller pores (<10 μm), suggesting the pore-size evolution observed could be largely a physical, rather than a chemical, effect, although the same result was observed in the relatively uncompressed material from southwestern Wisconsin. Anovitz et al. (2013a), however, argued for a chemical or flow-dominated origin. Several authors (e.g., Hedges and Whitelam, 2012; Wang et al., 2013) have argued that precipitation may be enhanced in smaller pores because of increased surface area of the pore wall, whereas others have shown that precipitation can also be enhanced in larger pores, either due to enhanced flow and transport or because precipitation in smaller pores is inhibited owing to increased surface energy of the precipitate (Prieto et al., 1990; Putnis et al., 1995; Putnis and Mauthe, 2001; Emmanuel and Berkowitz, 2007; Emmanuel and Ague, 2009; Emmanuel et al., 2010; Cook et al., 2011). Available data suggest that this difference may be process related and that both options or neither (Borgia, et al., 2012) can occur. Nonetheless, data obtained in this study clearly indicate that pore-size dependence needs to be considered in terms of the physical, as well as the chemical, processes to which a given rock unit is subjected.

ACKNOWLEDGEMENTS

Effort by L.M.A. was supported by research sponsored by the Division of Chemical Sciences, Geosciences, and Biosciences, Office of Basic Energy Sciences, U.S. Department of Energy. D.R.C. was funded by the Department of Energy Office of Basic Energy Sciences, Division of Chemical Sciences, Geosciences and Biosciences through the Energy Frontier Research Center - Nanoscale Control of Geologic CO_2. This research was also partially supported as part of the Center for Geologic Storage of CO_2, an Energy Frontier Research Center funded by the U.S. Department of Energy (DOE), Office of Science, Basic Energy Sciences (BES), under

Award Number DE-SC0C12504. We acknowledge the support of the National Institute of Standards and Technology, Center for Neutron Research, U.S. Department of Commerce, and the High-Flux Isotope Reactor at the Oak Ridge National Laboratory in providing the research neutron facilities used in this work. This work utilized facilities supported in part by the National Science Foundation under Agreement Number DMR-0944772. Certain commercial equipment, instruments, materials and software are identified in this paper to foster understanding. Such identification does not imply recommendation or endorsement by the National Institute of Standards and Technology, the Department of Energy, or the Oak Ridge National Laboratory, nor does it imply that the materials or equipment identified are necessarily the best available for the purpose. The authors have no pertinent commercial of other relationships that are known to them to create a conflict of interest.

References

Abramoff, M.D., Magalhaes, P.J. and Ram, S.J., 2004. Image processing with ImageJ. *Biophoton Int.* 11, 36–42.

Alefeld, B., Dohmen, L., Richter, D. and Brückel, T., 2000a. Space technology from X-ray telescopes for focusing SANS and reflectometry. *Physica B* 276–278, 52–54.

Alefeld, B., Dohmen, L., Richter, D. and Brückel, T., 2000b. X-ray space technology for focusing small-angle neutron scattering and neutron reflectometry. *Physica B* 283, 330–332.

Alefeld, B., Hayes, C., Mezei, F., Richter, D. and Springer, T., 1997. High-resolution focusing SANS with a toroidal neutron mirror. *Physica B* 234–236, 1052–1054.

Allen, A. J., 1991. Time-resolved phenomena in cements, clays and porous rocks. *J. Appl. Crystallogr.* 24, 624–634.

Amirjanov, A. and Sobolev, K., 2006. Fractal properties of Apollonian packing of spherical particles. *Model. Simul. Mater. Sci. Eng.* 14, 789–798.

Amirjanov, A. and Sobolev, K., 2012. Fractal dimension of Apollonian packing of spherical particles. *Adv. Powder Technol.* 23, 591–595.

Anishchik, S.V. and Medvedev, N.N., 1995. Three-dimensional Apollonian packing as a model for dense granular systems. *Phys. Rev. Lett.* 75, 4314-4317.

Anovitz, L.M. and Cole, D.R., 2015. Characterization and analysis of porosity and pore structures. *Rev. Miner. Geochem.* 80, 61–164.

Anovitz, L.M., Lynn, G.W., Cole, D.R., Rother, R., Allard, L.F., Hamilton, W.A., Porcar, L. and Kim, M.-H., 2009. A new approach to quantification of metamorphism using ultra-small and small angle neutron scattering. *Geochim. Cosmochim. Acta* 73, 7303–7324.

Anovitz, L.M., Rother, G. and Cole, D.R., 2011. Characterization of rock pore features in geothermal systems using small angle neutron scattering (SANS). *Proc. 36th Workshop Geotherm. Res. Eng. Sgp-Tr-191*. Stanford Univ., Stanford, CA, pp. 571–582.

Anovitz, L.M., Cole, D.R., Rother, G., Allard, Jr., L.F., Jackson A. and Littrell, K.C., 2013a. Diagenetic changes in macro- to nano-scale porosity in the St. Peter Sandstone: an (ultra) small angle neutron scattering and backscattered electron imaging analysis. *Geochim. Cosmochim. Acta.* 102, 280–305.

Anovitz, L.M., Wang, H.-W., Cole, D.R., Sheets, J., Rother, G., Faulder, D.D. and Walters, M., 2013b. Analysis of multiscale porosity at the Coso geothermal field. *Proc. 38th Workshop Geotherm. Res. Eng. SPG-TR-198*. Stanford Univ., Stanford, CA.

Anovitz, L.M., Cole, D.R., Jackson, A.J., Rother, G., Littrell, K.C., Allard, L.F., Pollington, A.D. and Wesolowski, D.J., 2015a. Effect of quartz overgrowth precipitation on the multiscale porosity of sandstone: a (U)SANS and imaging analysis. *Geochim. Cosmochim. Acta* 158, 199–222.

Anovitz, L.M., Cole, D.R., Sheets, J., Swift, A., Elston, H., Welch, S., Chipera, S.J., Littrell, K.C., Mildner, D.F.R. and Wasbrough, M.J., 2015b. Effects of maturation on multiscale (nm to mm) porosity in the Eagle Ford Shale. *Interpretations* 3, 1–11.

Athy, L.F., 1930. Density, porosity and compaction of sedimentary rocks. *AAPG Bull.* 14. 1–22.

Audet, D.M. and Fowler, A.C., 1992. A mathematical model for compaction in sedimentary basins. *Geophys. J. Int.* 110, 577–590.

Bahr, D.B., Hutton, E.W., Syvitski, J.P. and Pratson, L.F., 2001. Exponential approximations to compacted sediment porosity profiles. *Comput. Geosci.* 27, 691–700.

Barabási, S.-L. and Stanley, H.E., 1995. *Fractal Concepts in Surface Growth*. Cambridge University Press, New York. 388 pp.

Barker, J.G., Glinka, C.J., Moyer, J.J., Kim, M.H., Drews, A.R. and Agamalian, M., 2005. Design and performance of a thermal-neutron double-crystal diffractometer for USANS at NIST. *J Appl. Crystallogr.* 38, 1004–1011.

Barnes, D.A., Lundgren, C.E. and Longman, M.W., 1992. Sedimentology and diagenesis of the St. Peter Sandstone, Central Michigan Basin, United States. *AAPG Bull.* 76, 1507–1532.

Beard, D.C., and Weyl, P.K., 1973. Influence of texture on porosity and permeability of unconsolidated sand. *AAPG bulletin*, *57*(2), 349-369.

Biot, M.A., 1941. General theory of three-dimensional consolidation. *J. Appl. Phys.* 12, 155.

Block, A., von Bloh, W., Klenke, T. and Schellnhuber, H.J., 1991. Multifractal analysis of the microdistribution of elements in sedimentary structures using images from scanning electron microscopy and energy dispersive X-ray spectrometry. *J. Geophys. Res. B* 96, 16223–16230.

Borgia, A., Pruess, K., Kneafsey, T.J., Oldenburg, C.M. and Pan, L., 2012. Numerical simulation of salt precipitation in the fractures of a CO_2-enhanced geothermal system. *Geothermics* 44, 13–22.

Bulau, J.R., Waff, H.S. and Tyburczy, J.A., 1979. Mechanical and thermodynamic constraints on fluid distribution in partial melts. *J. Geophys. Res.* 84, 6102–6108.

Cercone, K.R., 1984. Thermal history of the Michigan Basin. *AAPG Bull.* 68, 130–136.

Cercone, K.R. and Pollack, H.N., 1991. Thermal maturity of the Michigan Basin. *Geol. Soc. Am. Spec. Pap.* 256, 1–12.

Cohen, M.H., 1987. The morphology of porous sedimentary rocks. In *Physics and Chemistry of Porous Media II: AIP Conf. Proc.* 154, 3–16.

Collinson, C., Sargent, M.L. and Jennings, J.R., 1988. Illinois basin region, In *Sedimentary Cover—North American Craton; U.S., The Geology of North America*, v. D-2 (ed. L. L. Sloss). Geological Society of America, Boulder, Colorado. pp. 383–426.

Cook, J.E., Goodwin, L.B. and Boutt, D.F., 2011. Systematic diagenetic changes in the grain-scale morphology and permeability of a quartz-cemented quartz arenite. *AAPG Bull.* 95, 1067–1088.

Daines, M.J. and Kohlstedt, D.L., 1997. Influence of deformation on melt topology in peridotites. *J. Geophys. Res.* 102, 10257–10271.

Dake, C.L., 1921. The problem of the St. Peter Sandstone. University of Missouri School of Mines and Metallurgy, Rolla, *Tech. Ser. 6, No. 1*., 225 p.

Dapples, E.C., 1955. General lithofacies relationship of St. Peter Sandstone and Simpson Group. *AAPG Bull.* 39, 444–467.

Debye, P., Anderson, Jr., H.R. and Brumberger, H., 1957. Scattering by an inhomogeneous solid. II. The correlation function and its application. *J. Appl. Phys.* 28, 679–683.

Desmond, K.W. and Weeks, E.R., 2014. Influence of particle size distribution on random close packing of spheres. *Phys. Rev. E* 90 (2), 022204.

Dott, R.H., 1964. Wacke, graywacke and matrix; what approach to immature sandstone classification? *J. Sediment. Res.* 34, 625–632.

Drzewiecki P.A., Simo, J.A., Brown, P.E., Castrogiovanni, E., Nadon, G.C., Shepherd, L.D., Valley, J.W., Vandrey, M.R., Winter, B.L. and Barnes, D.A., 1994. Sedimentology, diagenesis, and geochemistry of the Middle Ordovician St. Peter Sandstone of the Michigan Basin. In *Basin Compartments and Seals* (ed. P. Ortoleva). *AAPG Mem. 61*. AAPG, Tulsa, OK, pp. 179–200.

Elliott, W.C. and Aronson, J.L., 1987. Alleghenian episode of K-bentonite illitization in the southern Appalachian Basin. *Geology* 15, 735–739.

Elliott, W.C. and Aronson, J.L., 1993. The timing and extent of illite formation in Ordovician K-bentonites at the Cincinnati Arch, the Nashville Dome and north-eastern Illinois basin. *Basin Res.* 5, 125–135.

Emmanuel, S. and Berkowitz, B., 2007. Effects of pore-size controlled solubility on reactive transport in heterogeneous rock. *Geophys. Res. Lett.* 34, L06404.

Emmanuel, S. and Ague, J.J., 2009. Modeling the impact of nano-pores on mineralization in sedimentary rocks. *Water Resour. Res.* 45, W04406.

Emmanuel, S., Ague, J.J. and Walderhaug, O., 2010. Interfacial energy effects and the evolution of pore size distributions during quartz precipitation in sandstone. *Geochim. Cosmochim. Acta* 74, 3539– 3552.

Evertsz, C.J.G. and Mandelbrot, B.B., 1992. Multifractal measures. In *Chaos and Fractals: New Frontiers of Science* (eds. H. Peitgen, H. Jürgens and D. Saupe). Springer, Berlin, 984 pp., Appendix A2.

Farver, J.R. and Yund, R.A., 1992. Oxygen diffusion in a fine-grained quartz aggregate with wetted and nonwetted microstructures. *J. Geophys. Res.: Solid Earth* 97 (B10), 14017–14029.

Farver, J.R. and Yund, R.A., 1995. Grain boundary diffusion of oxygen, potassium and calcium in natural and hot-pressed feldspar aggregates. *Contrib. Miner. Petrol.* 118, 340–355.

Fishman, N.S., 1997. Basin-wide fluid movement in a Cambrian paleoaquifer: evidence from the Mt. Simon sandstone, Illinois and Indiana. in Montanez, J.P., Gregg, M., and Shelton, K.L., eds., Basin-wide diagenetic patterns: SEPM (Society for Sedimentary Geology) Special Publication No. 57, p. 221-234.

Fisher, J.H., Barratt, M.W., Droste, J.B. and Shaver, R.H., 1988. Michigan Basin. In *Sedimentary Cover—North American Craton; U.S., The Geology of North America*, v. D-2 (ed. L. L. Sloss). Geological Society of America, Boulder, CO, pp. 361–382.

Fishman, N.S., 1997. Basinwide fluid movement in a Cambrian paleoaquifer: Evidence from the Mt. Simon Sandstone, Illinois and Indiana, *in* I.P. Montenez, J.M. Gregg, and K.L. Shelton, eds., Basinwide diagenetic patterns: Integrated petrologic, geochemical, and hydrologic considerations: Society for Sedimentary Geology (SEPM), Special Publication, v. 57, p. 221-234

Folk, R.L., 1951. Stages of textural maturity in sedimentary rocks. *J. Sediment. Pet.* 21, 127–130.

Folk, R.L., 1961. *Petrology of Sedimentary Rocks*. Hemphill's Book Store, Austin, TX, 154 pp.

Fowler, A.C. and Yang, X.S., 1998. Fast and slow compaction in sedimentary basins. *SIAM J. Appl. Math.* 59, 365–385.

Freiburg, J.T., Morse, D.G., Leetaru, H.E., Hoss, R.P. and Yan, Q., 2014. A depositional and diagenetic characterization of the Mt. Simon Sandstone at the Illinois Basin – Decatur Project carbon capture and storage site, Decatur, Illinois, USA. *Circ. 583*. Illinois State Geological Survey, Champaign, 59 pp. and 3 digital appendices.

Freiburg, J.T., Ritzi, R.W. and Kehoe, K.S., 2016), Depositional and diagenetic controls on anomalously high porosity within a deeply buried CO_2 storage reservoir—The Cambrian Mt. Simon Sandstone, Illinois Basin, USA. *Int. J. Greenh. Gas Control*, 55, 42-54

Girard, J.P. and Barnes, D.A., 1995. Illitization and paleothermal regimes in the Middle Ordovician St. Peter Sandstone, Central Michigan Basin; K-Ar, oxygen isotope, and fluid inclusion data. *AAPG Bull.* 79, 49–69.

Graham, C.M., Valley, J.W. and Winter, B.L., 1996. Ion microprobe analysis of $^{18}O/^{16}O$ in authigenic and detrital quartz in the St. Peter Sandstone, Michigan Basin and Wisconsin Arch, USA: contrasting diagenetic histories. *Geochim. Cosmochim. Acta* 60, 5101–5116.

Grathoff, G.H., Moore, D.M., Hay, R.L., and Wemmer, K., 2001. Origin of illite in the lower Paleozoic of the Illinois basin: evidence for brine migrations. *Geological Society of America Bull.* 113 (8), 1092-1104.

Hay, R.L. and Liu J., 1994. Potassic mineralization in the Mississippi Valley: mineralogic and oxygen isotope constraints on fluid temperatures. In *Basin-Wide Diagenetic Patterns: Integrated Petrologic, Geochemical, and Hydrologic Considerations: Program, Abstracts, and Field Guide, Society for Sedimentary Geology Research Conference, Lake Ozark, Mo.* (eds. J. M. Gregg, I. P. Montanez, and K. L. Shelton). Society for Sedimentary Geology, Tulsa, OK, 31 pp.

Hay, R.L., Lee M., Kolata, D.R., Matthews, J.C. and Morton, J.P., 1988. Episodic potassic diagenesis of Ordovician tuffs in the Mississippi Valley area. *Geology* 16, 743–747.

Hedges, L.O. and Whitelam, S., 2012. Selective nucleation in porous media. *Soft Matter* 9, 9763–9766.

Herrmann, H.J., Mantica, G. and Bessis, D., 1990. Space-filling bearings. *Phys. Rev. Lett.* 65, 3223–3226.

Hillel D., 1980. *Fundamentals of Soil Physics*. Academic Press, Cambridge, MA, 413 pp.

Hinze, W.J., and Braile, L.W., 1988. Geophysical aspects of the craton: U.S., in Sloss, L.L. ed, Sedimentary Cover-North American Craton; U.S.: Boulder Colorado, Geological Society of America, The Geology of North America, V. D-2

Hiraga, T., Nishikawa, O., Nagase, T. and Akizuki, M., 2001. Morphology of intergranular pores and wetting angles in pelitic schists studied by transmission electron microscopy. *Contrib. Miner. Petrol.* 141, 613–622.

Hoholick, J.D., Metarko, T. and Potter, P.E., 1984. Regional variations of porosity and cement: St. Peter and Mount Simon Sandstones in Illinois Basin. *AAPG Bull.* 68, 753–764.

Hu, Q., Ewing, R.P., and Dultz, S, 2012. Low pore connectivity in natural rock, Journal of Contaminant Hydrology, 133 (2012) 76–83

Hutton, J., 1788. Theory of the Earth; or an investigation of the laws observable in the composition, dissolution, and restoration of land upon the Globe. *Trans. R. Soc. Edinb.* 1, 209–304.

Hyodo, A., Kozdon, R., Pollington, A.D. and Valley, J.W., 2013. Evolution of quartz cementation and burial history of the Eau Claire Formation based on *in situ* oxygen isotope analysis of quartz overgrowths. *Chem. Geol.* 384, 168–180.

Ilavsky, J. and Jemian, P.R., 2009. Irena: tool suite for modeling and analysis of small-angle scattering. *J. Appl. Crystallogr.* 42, 347–353.

Kelly, J.L., 2006. Silcrete in the St. Peter Sandstone. M. S. thesis, Univ. Wisconsin–Madison, 124 pp.

Kelly, J.L., Fu, B., Kita, N.T. and Valley, J.W., 2007. Optically continuous silcrete quartz cements of the St. Peter Sandstone: high precision oxygen isotope analysis by ion microprobe. *Geochim. Cosmochim. Acta* 71, 3812–3832.

Kline, S.R., 2006. Reduction and analysis of SANS and USANS data using Igor Pro. *J. Appl. Crystallogr.* 39, 895–900.

Kolata, D.R., 2010. Cambrian and Ordovician Systems (Sauk and Tippecanoe II Subsequence). In *The Geology of Illinois* (eds. D. R. Kolata and C. K. Nimz). Illinois State Geological Survey, Champaign, pp. 136–157.

Kolata, D.R. and Nelson, J.W., 2010. Tectonic history. In *Geology of Illinois* (eds. D. R. Kolata and C. K. Nimz). Illinois State Geological Survey, Champaign, pp. 77–89.

Krueger, H.W. and Woodard, H.H., 1972. Potassium-argon dating of sanidine-rich beds in the St. Peter Sandstone, Wisconsin. *Geol. Soc. Am. Abstr. Progr.* 4, 568–569.

Kruhl, J.H. and Nega, M., 1996. The fractal shape of sutured quartz grain boundaries: application as a geothermometer. *Geologische Rundschau* 85, 38–43.

Kruhl, J.H., Wirth, R. and Morales, L.F.G., 2013. Quartz grain boundaries as fluid pathways in metamorphic rocks: quartz grain boundaries. *J. Geophys. Res.: Solid Earth* 118, 1957–1967.

Kutílek, M., Jendele, L. and Panayiotopoulos, K., 2006. The influence of uniaxial compression upon pore size distribution in bi-modal soils. *Soil Tillage Res.* 86, 27–37.

Laporte, D. and Watson, E.B., 1991. Direct observation of near-equilibrium pore geometry in

synthetic quartzites at 600–800°C and 2–10.5 Kbar. *J. Geol.* 99, 873–878.

Lee, M.K. and Aronson, J.L., 1991. Repetitive occurrence of potassic diagenesis in the region of the Upper Mississippi Valley (UMV) mineral district: implications for a persistent paleo-hydrological setting favorable for diagenesis. *28th Annu. Meet. Progr. Abstr. 98*. Clay Minerals Society, Chantilly, VA.

Lee, V.W., Mackwell, S.J. and Brantley, S.L., 1991. The effect of fluid chemistry on wetting textures in novaculite. *J. Geophys. Res.: Solid Earth* 96 (B6), 10023–10037.

Littrell, K.C., Atchley, K.M., Cheng, G., Melnichenko, Y.B. and Wignall, G.D., 2008. General purpose small-angle neutron scattering instrument on HFIR Oak Ridge. *Neutron News* 19 (3), 20–21.

Mai, H. and Dott, Jr., R.H., 1985. A subsurface study of the St. Peter Sandstone in southern and eastern Wisconsin. *Wis. Geol. Nat. Hist. Surv. Inf. Circ. 47*. Wisconsin Geological and Natural History Survey, Madison, 26 pp.

Majumder, S. and Mamtani, M.A., 2009). Fractal analysis of quartz grain boundary sutures in a granite (Malanjkhand, central India)—Implications to infer regional tectonics. *J. Geol. Soc. India* 73, 309–319.

Makowitz, A., Lander, R.H. and Milliken, K.L., 2006. Diagenetic modeling to assess the relative timing of quartz cementation and brittle grain processes during compaction. *AAPG Bull.* 90, 873–885.

Mamtani, M.A. and Greiling, R.O., 2010. Serrated quartz grain boundaries, temperature and strain rate: testing fractal techniques in a syntectonic granite. *Geol. Soc. Lond. Spec. Publ.* 332 (1), 35–48.

Mancktelow, N.S., Grujic, D. and Johnson, E.L., 1998. An SEM study of porosity and grain boundary microstructure in quartz mylonites, Simplon Fault Zone, central Alps. *Contrib. Mineral. Petrol.* 131 (1), 71–85.

Mandelbrot, B., 1977. *Fractals: Form, Chance and Dimension*. W. H. Freeman, New York, 365 pp.

Mandelbrot B.B., 1982. *The Fractal Geometry of Nature*. W. H. Freeman, New York. 468 pp.

Mandelbrot, B.B., 1989. Multifractal measures, especially for the geophysicist. *Pure Appl. Geophys.* 131, 5–42.

Marshall, B.D., Woodard, H.H. and DePaolo, D.J., 1986. K-Ca-Ar systematics of authigenic sanidine from Waukau, Wisconsin, and the diffusivity of argon. *Geology* 14, 936–938.

Merrit, M. and Zhang, Y., 2004. An interior-point gradient method for large-scale totally nonnegative least squares problems. *Tech. Rep. TR04-08*. Department of Computational and Applied Mathematics, Rice University, Houston, Texas. http://www.caam.rice.edu/caam/trs/2004/TR04-08.pdf.

Nimmo, J.R., 2004. Porosity and pore size distribution. In *Encyclopedia of Soils in the Environment* (ed. D. Hillel). Elsevier, Amsterdam. pp. 295–303.

Nimmo, J.R., 2013. Porosity and pore size distribution? In *Reference Module in Earth Systems and Environmental Sciences* (ed. Scott A. Elias). Elsevier, Amsterdam. doi:10.1016/B978-

0-12-409548-9.05265-9.

Owen, D.D., 1847. Preliminary report of the geological survey of Wisconsin and Iowa. *U.S. Gen. Land Office Rept., Congr. Docs., 30th Congr., 1st session, S. Ex. Doc. 2*, pp. 160–173.

Parasnis, D.S., 1960. The compaction of sediments and its bearing on some geophysical problems. *Geophys. J. Int.* 3, 1–28.

Pettijohn, F.J., Potter, P.E. and Siever, R., 2012. *Sand and Sandstone*. Springer Science and Business Media, New York.

Pitman, J.K. and Spöetl, C., 1996. Origin and timing of carbonate cements in the St. Peter Sandstone, Illinois Basin: evidence for a genetic link to Mississippi Valley-type mineralization. In Siliciclastic Diagenesis and Fluid Flow: Concepts and Applications (Eds. L. J. Crossey, R. Loucks and M. W. Totten). *J. Sediment. Geol. Spec. Publ.* 55, 87–203.

Pitman, J.K., Goldhaber, M.B. and Spoetl, C., 1997. Regional diagenetic patterns in the St. Peter Sandstone: implications for brine migration in the Illinois Basin. *U.S. Geol. Surv. Bull.2094-A*, U.S. Geological Survey, Denver, CO, pp. 17–18.

Playfair, J., 1802. *Illustrations of the Huttonian Theory of the Earth*. Cambridge University Press, Cambridge, UK.

Pollington, A.D., Kozdon, R. and Valley, J.W., 2011. Evolution of quartz cementation during burial of the Cambrian Mount Simon Sandstone, Illinois Basin: in situ microanalysis of $\delta^{18}O$. *Geology* 39, 1119–1122.

Pouya, A., Djéran-Maigre, I., Lamoureux-Var, V. and Grunberger, D., 1998. Mechanical behaviour of fine grained sediments: experimental compaction and three-dimensional constitutive model. *Mar. Petrol. Geol.* 15, 129–143.

Prieto, M., Putnis, A. and Fernandez-Diaz, L., 1990. Factors controlling the kinetics of crystallization: supersaturation evolution in a porous medium: application to barite crystallization. *Geol. Mag.* 127, 485–495.

Prothero, D.R. and Dott, Jr., R.H., 2004. *Evolution of the Earth*, seventh ed. McGraw-Hill, New York.

Putnis, A. and Mauthe, G., 2001. The effect of pore size on cementation in porous rocks. *Geofluids* 1, 37–41.

Putnis, A., Prieto, M. and Fernandez-Diaz, L., 1995. Fluid supersaturation and crystallization in porous media. *Geol. Mag.* 132, 1–13.

Rasband, W.S., 1997–2016. ImageJ. U.S. National Institutes of Health, Bethesda, Maryland. http://imagej.nih.gov/ij/.

Rowan, E.L. and Goldhaber, M.B., 1996. Fluid inclusions and biomarkers in the Upper Mississippi Valley zinc–lead district; implications for the fluid-flow and thermal history of the Illinois Basin. *U.S. Geol. Surv. Bull. 2094-F*. U.S. Geological Survey, Denver, CO, 34 pp.

Royne, A. and Jamtveit, B., 2015. Pore-scale controls on reaction. *Rev. Miner. Geochem.* 80, 25–44.

Rubey, W.W. and Hubbert, M.K., 1959. Role of fluid pressure in mechanics of overthrust faulting:

II. Overthrust belt in geosynclinal area of western Wyoming in light of fluid-pressure hypothesis. *Geol. Soc. Am. Bull.* 70, 167–206.

Schneider, C.A., Rasband, W.S. and Eliceiri, K.W., 2012. NIH Image to ImageJ: 25 years of image analysis. *Nat. Methods* 9, 671–675.

Schneider, F., 1993. Modele de compaction elasto-plastique en simulation de bassins. *Reaue de l'Institut Francais du Pétrole* 48, 1–14.

Schneider, F., Potdevin, J.L., Wolf, S. and Faille, I., 1996. Mechanical and chemical compaction model for sedimentary basin simulators. *Tectonophysics* 263, 307–317.

Sedgwick, A. and Murchison, R.I., 1840. On the physical structure of Devonshire, and on the subdivisions and geological relations of its older stratified deposits, etc. *Trans. Geol. Soc. Lond.*, ser. 2, vol. 5 (part II): 633–687 (part I) and 688–704 (part II).

Shi, Y. and Wang, C.-Y., 1986. Pore pressure generation in sedimentary basins: overloading versus aquathermal. *J. Geophys. Res.* 91 (B2), 2153–2162.

Skempton, A.W., 1944. Notes on the compressibility of clays. *Q. J. Geol. Soc.* (*Lond.*) 100, 119–135.

Sliwinski, M., Kozdon, R., Kitijima, K., Denny, A. and Valley, J.W., 2016. Microanalysis of carbonate cement $\delta^{18}0$ in a CO_2 storage system seal: insights into the diagenetic history of the Eau Claire Formation (Upper Cambrian), Illinois Basin. *AAPG Bull.* 100, 1003–1031.

Smith, J.E., 1971. The dynamics of shale compaction and evolution in pore-fluid pressures. *Math. Geol.* 3, 239–263.

Sohn, H.Y. and Moreland, C., 1968. The effect of particle size distribution on packing density. *Can. J. Chem. Eng.* 46, 162–167.

Stack, A.G., 2015. Precipitation in pores: a geochemical frontier. *Rev. Miner. Geochem.* 80, 165–190.

Sweeney, J.J. and Burnham, A.K., 1989. A chemical kinetic model of vitrinite maturation and reflection. *Geochim. Cosmochim. Acta* 53, 2649–2657.

Takei, Y., 2010. Stress-induced anisotropy of partially molten rock analogue deformed under quasi-static loading test. *J. Geophys. Res.* 115, B03204.

Takei, Y. and Katz, R.F., 2013. Consequences of viscous anisotropy in a deforming, two-phase aggregate. Part 1. Governing equations and linearized analysis. *J. Fluid Mech.* 734, 424–455.

Terzaghi, K., 1923. Die berechnung der durchlässigkeitsziffer des tones aus dem verlauf der hydrodynamischen spannungsercheinungen. Sitzungsber. *Akad. Wiss. Wien* 132 (IIa), 125-138.

Toramaru, A. and Fujii, N., 1986. Connectivity of melt phase in a partially molten peridotite. *J. Geophys. Res.* 91, 9239–9252.

Von Bargen, N. and Waff, H.S., 1986. Permeabilities, interfacial areas and curvatures of partially molten systems: results of numerical computation of equilibrium microstructures. *J. Geophys. Res.* 91, 9261–9276.

Waff, H.S. and Bulau, J.R., 1979. Equilibrium fluid distribution in an ultramafic partial melt under hydrostatic stress conditions. *J. Geophys. Res.* 84, 6109–6114.

Wang, H.-W., Anovitz, L.M., Burg, A., Cole, D.R., Allard, L.F., Jackson, A.J., Stack, A.G. and Rother, G., 2013. Multi-scale characterization of pore evolution in a combustion metamorphic complex, Hatrurim basin, Israel: combining (ultra) small-angle neutron scattering image analysis. *Geochim. Cosmochim. Acta* 121, 339–362.

Watson, E.B. and Brenan, J.M., 1987. Fluids in the Lithosphere, 1. Experimentally-determined wetting characteristics of CO_2-H_2O fluids and their implications for fluid transport, host-rock physical properties, and fluid inclusion formation. *Earth Planet. Sci. Lett.* 85, 497–515.

Williams, H., Turner, F.J. and Gilbert, C.M., 1954. *Petrography*. W. H. Freeman, San Francisco, CA, 406 pp.

Wong, P.-Z., 1985. Scattering by inhomogeneous systems with rough internal surfaces—porous solids and random-field Ising systems. *Phys. Rev. B* 32, 7417–7424.

Wong, P.-Z., Howard, J. and Lin, J.-S., 1986. Surface roughening and the fractal nature of rocks. *Phys. Rev. Lett.* 57, 637–640.

Zdan, S.A., 2013. Stratigraphic controls on diagenetic pathways in the St. Peter Sandstone, Michigan Basin. M.S. Thesis, Western Michigan Univ., Kalamazoo, 132 pp.

Zimmerman, M.E., Zhang, S.Q., Kohlstedt, D.L. and Karato, S., 1999. Melt distribution in mantle rocks deformed in shear. *Geophys. Res. Lett.* 26, 1505–1508.